Laser and Particle Beams (2001), *19*, 323–343. Printed in the USA.

Two- and three-dimensional modeling of the different phases of wire-array *z*-pinch evolution

J.P. CHITTENDEN, S.V. LEBEDEV, S.N. BLAND, J. RUIZ-CAMACHO,
F.N. BEG, AND M.G. HAINES
Blackett Laboratory, Imperial College, London SW7 2BZ, UK

(RECEIVED 22 May 2000; ACCEPTED 22 February 2001)

Abstract

A series of specialized multidimensional resistive magnetohydrodynamic (MHD) models have been developed to tackle the different phases of evolution of wire array *z*-pinch implosions. Two-dimensional (r–z) "cold-start" or "wire initiation" simulations of single wires indicate the persistence of a two-component structure with a cold, dense core embedded within a much hotter, low density, $m = 0$ unstable corona. Cold-start simulations with similar conditions to wires in an array show a general trend in the plasma structure from discrete wires with large $m = 0$ perturbation amplitudes to partially merged wires with smaller perturbation amplitudes as the number of wires is increased. Two-dimensional (r–θ) simulations then show how the persistence of dense wire cores results in the injection of material between the wires into the interior of the array, generating radial plasma streams which form a precursor plasma upon reaching the axis. Higher-resolution 2-D (r–θ) simulations show similar behavior for large number wire arrays in use at Sandia National Laboratories. This model is also used to predict which modes of implosion are in operation in nested wire array experiments. Separate r–θ plane simulations of the flux of plasma imploding towards the axis from the outer array and the bombardment of the inner array by this flux are presented. Finally, 2-D (r–z) simulations of the Rayleigh–Taylor instability during the final implosion phase are used to illustrate the effect upon the power and duration of the radiation output pulse. The results of low-resolution 3-D resistive MHD simulations are also presented. The need for much higher resolution 3-D simulations of certain aspects of wire array evolution is highlighted.

1. INTRODUCTION AND BACKGROUND

Despite the recent spectacular increases in X-ray power obtained from wire array *z* pinches (Sanford *et al.*, 1996; Deeney *et al.*, 1998), achieving high yield fusion in a *z*-pinch-driven hohlraum will require still further substantial increases in both X-ray power and yield (Hammer *et al.*, 1999). Being able to design optimal load configurations which maximize the power output would significantly reduce the cost of future generators designed for high-yield experiments. However, the factors that limit the X-ray power in present generation experiments are still not well understood. The two main limiting factors are thought to be the slow rate of wire ablation, which leads to injection of mass into the interior of the array prior to implosion and the development of the Rayleigh–Taylor instability. Computational modeling of these phenomena can be extremely complex due to the intrinsically three-dimensional (3-D) nature of the problem. While 3-D resistive MHD codes are now becoming available, simulations of the entire experiment with adequate spatial resolution remains unfeasible. In this paper, we present an alternative approach, which is to model different phases of the evolution using different specialized two-dimensional (2-D) and 3-D models and attempt to link them together to form a composite model of the whole experiment. This has the added advantage that this series of simpler problems can be more readily compared to experiments for the all important code verification.

We continue Section 1 by describing the different stages of wire array *z*-pinch evolution and describing low-resolution 3-D modeling of the implosion. In Section 2 we describe 2-D "cold-start" or "wire initiation" calculations of single wires, showing how the passage of current begins the plasma formation process but also excites the $m = 0$ instability in each wire. The results of this section are then used in Section 3 to initialize 2-D simulations in the r–θ plane which show how the mass injected between the wires determines the radial profile for the implosion. This model is also used, in Section 4, to explore the different modes of collision between nested wire arrays. In Section 5, the results of the two models described in Sections 2 and 3 are then used to

Address correspondence and reprint requests to: J.P. Chittenden, Blackett Laboratory, Imperial College, London SW7 2BZ, United Kingdom. E-mail: j.chittenden@ic.ac.uk

construct the radial and axial structure of the plasma for 2-D simulations in the r–z plane which model the Rayleigh–Taylor instability during the final implosion phase.

1.1. The different phases of wire array z-pinch evolution

In each wire in the array, as in single wire z-pinch experiments, the initial flow of current heats the wire material up to the vaporization temperature, at which point it begins to expand. Ionization of the lower density surface regions is followed by rapid heating and expansion of this region resulting in the formation of a low density plasma corona which surrounds a much higher density cold core. Numerous experiments in both single wires (Figura *et al.*, 1991; Kalantar & Hammer, 1993; Beg *et al.*, 1997; Guskov, 1998; Ivanenkov, 1998; Lebedev *et al.*, 1998*a*; Pikuz *et al.*, 1999; Ruiz-Camacho *et al.*, 1999) and in wire arrays (Deeney *et al.*, 1997; Lebedev *et al.*, 1998*b*, 1999) have observed this two-component structure persisting until late into the discharge. Once the magnetic field generated by the rising current becomes large enough, the low-density corona begins to self-pinch onto the core. In the case of single wires, this pinching results in the growth of $m = 0$ instabilities which are cylindrically symmetric about the axis of the wire. In the case of wire arrays, the self-pinching forces the coronal plasma to adopt the characteristic "tear-drop" shape of the total magnetic field that has components both due to the private flux associated with each wire and the global flux of the whole array. The instability growth in this plasma is then $m = 0$-like but with a noncircular cross section. The high density of the wire cores and the low level of current flowing in them means that they remain stationary until late into the discharge. The $\mathbf{J} \times \mathbf{B}_{global}$ force then acts solely on the low-density plasma coronas, pushing this material through the gaps between the wire cores and injecting it into the interior of the array in the form of radial plasma streams. Merger of low-density plasma from adjacent wires in the interwire gap occurs early on. The density of this material is, however, too low to prevent it from being swept inside the array. In wire arrays with small interwire gaps, the density to which the plasmas merge can become high enough to extinguish the mass injection process but this does not usually occur in most wire arrays in use today. At roughly half the final implosion time, the radial streams of plasma reach the axis, forming a precursor plasma. The continuous bombardment of this precursor by streams of material from the wires provides a confining force that sustains the high density of the precursor up until the final implosion. Eventually the fraction of the mass remaining in the wire cores begins to implode and is accelerated towards the axis by the magnetic field. This acceleration is susceptible to the development of magneto-Rayleigh–Taylor (MRT) instabilities. The most probable source of seed perturbation for the global MRT is the statistical average (Haines, 1998) of $m = 0$-like instabilities growing in the coronal plasmas around each wire. The final stagnation phase usually consists of an inhomogeneous plasma containing a fraction of the mass impacting at high speed onto a stationary precursor.

The approach to modeling wire arrays described here is to treat the plasma formation phase, the mass injection phase, and the Rayleigh–Taylor instability phase independently using different models and to use the results from one simulation to provide the initial conditions for the next simulation. This treatment is, of course, fundamentally flawed in that the phases are not distinct and cannot be described independently. For example, the wire core ablation process is still in progress during the mass injection phase and in some instances during the Rayleigh–Taylor instability development phase as well. It would be far more desirable to treat the full process in three dimensions. While high-resolution 3-D simulations of the full array are highly impractical, 3-D simulations of a few of the wires in the array may offer the key to bridging the gap between the different phases of evolution. Work on such simulations is currently in progress.

1.2. Low resolution 3-D results

Figure 1 shows a series of iso-density contours from a low resolution simulation of an array of eight, 15-μm-diameter aluminum wires on MAGPIE, using the 3-D resistive MHD code described in Section 2.2 with 200-μm cubic cells. Only two of the eight wires are simulated, with the axis of symmetry to the back and right. The axial dimension has been stretched to allow better visualization. A number of the key

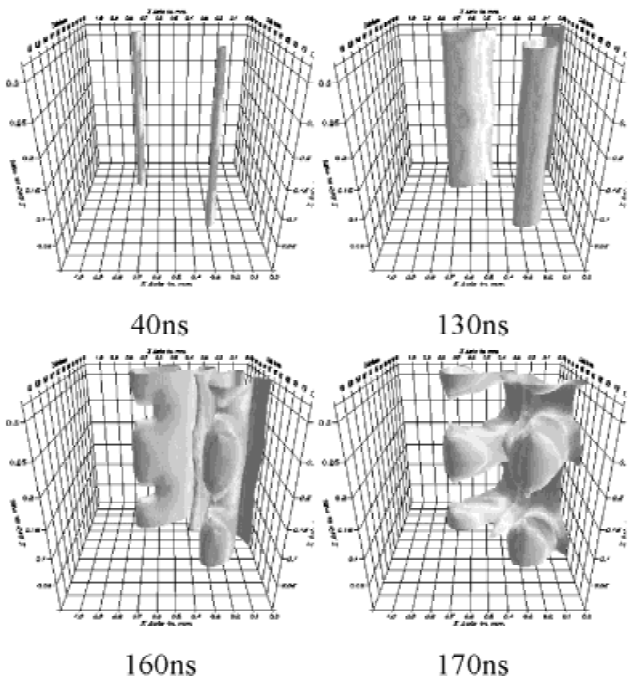

Fig. 1. A series of iso-density contours from a low-resolution 3-D simulation of an array of 8 15-μm-diameter aluminum wires on MAGPIE.

https://doi.org/10.1017/S0263034601193031 Published online by Cambridge University Press

features described above can be seen. First the persistence of dense wire cores results in radial plasma streams which exhibit the characteristically teardrop shaped cross section and which form the precursor plasma on the axis. At later times, the rapid growth of the Rayleigh–Taylor instability can be seen. Here, however, the instability grows from a long wavelength (2 mm) harmonic perturbation which was applied at the beginning of the run. The low spatial resolution does not allow us to follow the evolution of the instability from shorter wavelength random perturbations as desired, nor does it allow the behavior of the wires during ablation to be resolved. Therefore despite representing two weeks of run time on a fast workstation, this simulation is merely illustrative rather than predictive.

The results in Figure 1 do, however, illustrate a fundamental difference in the evolution of the Rayleigh–Taylor instability compared to the 2-D (r–z) results (described in Section 5) for arrays in which the dense wire cores persist until the final implosion phase (see Section 3). In Figure 1, the rapid implosion of material between 160 and 170 ns occurs only at regions along the length of the wire where the mass-per-unit length is low. Once this motion occurs, it essentially "breaks" the wires and allows the majority of the current to penetrate inside the remaining wire cores, which accelerates the broken regions rapidly down to the axis. The regions of wire cores that were not in motion before this time are now essentially bypassed by the current and remain stationary until well after peak emission. The plasma structure at 170 ns does indeed resemble a Rayleigh–Taylor structure but with the spikes now "anchored" to the original positions of the wires. However, it is quite likely that the kinetic energy of the small amount of material in motion between 160 and 170 ns is insufficient to account for the radiation obtained. In fact the radiation may well occur as a result of the breaking of the wires, which allows the current to penetrate down to the axis and compress the large fraction of material which has already accumulated there.

2. "COLD START" MODELING OF WIRE INITIATION AND PLASMA FORMATION IN SINGLE WIRES

At first sight, determining the time at which complete vaporization and ionization of such wires occurs seems to be a simple matter of calculating the rate of energy deposition into the wire material. Consider 2-cm-long, 7.5-μm-diameter tungsten wires with current rising in each wire at 1 kA per nanosecond (parameters which are typical of many wire array experiments). Since the skin depth greatly exceeds the wire radius, ohmic heating of the wire is at first volumetric. Using the resistivity model described below, the 78 mJ required to heat the wire material to the vaporization temperature and to provide the latent heats of fusion and evaporation is deposited in the first 0.75 ns. To deposit the further 83 mJ required to heat the material to ionization temperatures and to provide the first ionization energy takes a further 0.15 ns. Therefore, compared to the 100-ns time scale of the current rise, we would expect the entire array mass to become plasma almost instantaneously. This scenario does not, however, take into account the inhomogeneities with which phase transitions occur. Once the surface vapor starts to expand into the vacuum, its density drops and hence this is where ionization first occurs, forming a low-density plasma corona. While the resistivity of this plasma is comparable to that of the liquid/vapor core, the cross-sectional area of the corona is much greater than that of the core, and, hence, the majority of the current is switched to the corona. Since the density and therefore the specific heat capacity of the corona are low, ohmic heating results in a rapid temperature rise and fast expansion of surface plasma. Therefore, within a few nanoseconds of current start, the region of energy deposition has been moved away from the reservoir of cold core material. Any further ionization of the core material relies on the diffusion of thermal energy and magnetic flux from the corona into the core. Since the time-scale for diffusion can be a significant fraction of the current rise time, the liquid/vapor core ionizes slowly and can persist until late into the discharge.

2.1. Equations of state and transport coefficients

During the solid and liquid phases, the wire material remains virtually stationary and holds together. At the vaporization temperature of aluminum, the pressure of a perfect gas at solid density is $\sim$20 kbar. The electrons in this material do not, however, behave as a perfect gas. In condensed phases, exchange effects act as a binding force so that little or no pressure is exerted by the electrons. Even in the vapor state, at high enough densities and low enough temperatures, the pressure and internal energy of the electron fluid are substantially reduced with respect to the perfect gas values. The behavior of the condensed states of matter can be emulated in a fluid simulation by modifying the equations of state to include degeneracy, nuclear potential, and exchange effects. In the work presented here, we use analytic approximations to Latter's results (Latter, 1955) for a Thomas-Fermi model of the electrons to determine the internal energy, pressure and energy derivatives ($\partial U/\partial T$ and $\partial U/\partial \rho$) as functions of the density and temperature. Corrections to include quantum and exchange effects (Kirzhnits, 1959) then allow the condensed phases to be modeled. This equation-of-state model was originally developed by A.R. Bell in 1980 and has been used extensively in the 1-D Lagrangian laser-plasma hydrodynamics code MEDUSA (Christiansen *et al.*, 1974).

Figure 2 shows the electron pressure in aluminum calculated by this model as a function of density, for various temperatures. At high temperatures and low densities, the straight-line dependence is indicative of perfect gas behavior. At very high densities, the pressure is increased over the perfect gas value, eventually becoming a function of density only as the electrons become degenerate. For low tempera-

https://doi.org/10.1017/S0263034601193031 Published online by Cambridge University Press

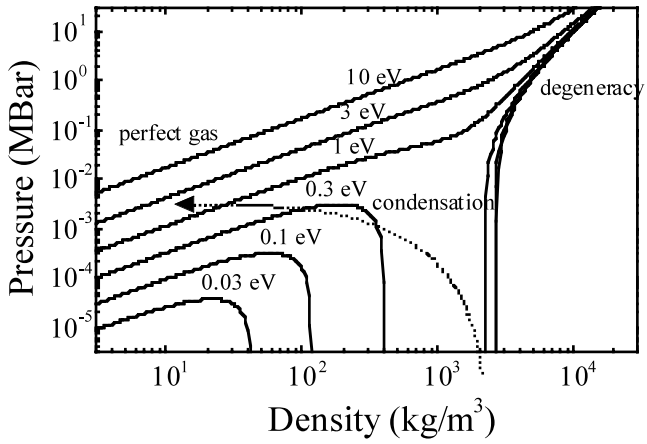

Fig. 2. Electron pressure *versus* density for various temperatures provided by the equation-of-state model. A typical trajectory (dotted line), for material ablated from the core and expanding out into the corona, is shown.

tures around solid density, the electron pressure becomes negative, thus modeling a condensed phase. In practice, the ions are still treated with the perfect gas equation of state and a minimum electron pressure is set so that the minimum total pressure is zero. The model represents a generic equation of state with no knowledge of the details of each phase transition and how these differ with material. The solid density of the material is, however, used as an input parameter in order to establish the relative importance of the correction terms. Comparison to the Los Alamos SESAME database indicates good agreement in general; however, the analytic approximations used become inaccurate at very low temperatures and densities.

Material ablated from the core and expanding out into the corona emerges from the condensed phase towards the perfect gas regime, following a trajectory similar to the example superimposed on Figure 2, with degeneracy playing little part in the problem. The strong gradients in Figure 2 mean that small changes in density and temperature can result in large pressure changes. Using the value of $\partial U/\partial \rho$ returned by the equation-of-state model to determine the sound speed and hence the time-step usually eliminates numerical instabilities.

To calculate the diffusion of magnetic field, the energy deposition by ohmic heating, and energy transfer by thermal conduction, it is essential to include accurate electrical resistivities and thermal conductivities that span a wide range of different material parameters and states. At low temperatures, the resistivity of the solid and liquid phases of metals and their rate of increase with temperature is well established (Dyos & Farrell, 1992). In the high-temperature and low-density well-ionized plasma limit, the resistivity of plasma adopts the well-established Spitzer-like dependence of $T^{-3/2}$. Between these two well-established limits, around the implied resistivity maximum at 1 to 10 eV, there is considerable uncertainty (particularly at densities lower than solid) with more than an order of magnitude difference between theoretical models. For this work, we adopt a model based on the dense plasma electron conductivity model of Lee and More (1984). The electron mean free path used to calculate the electron relaxation time in the condensed phase [Equations 32 and 33 in Lee & More (1984)], is modified to include a different minimum temperature for each metal used. This provides a mechanism for numerically fitting the resistivity model to the known behavior at low temperature and solid density and results in somewhat higher resistivities in the condensed phases than in Lee and More (1984). Similar but more comprehensive modifications to Lee and More's model are described in an article by Desjarlais (2001).

2.2. Description of the 2-D (*r*–*z*) resistive MHD code

These equations of state and transport coefficients were incorporated into a 2-D (*r*–*z*) resistive MHD code (which is described in more detail in Chittenden *et al.*, 1997*b* and 2000). Explicit hydrodynamics is performed on an Eulerian grid using second-order Van Leer advection (as interpreted by Youngs, 1982). Reflective boundary conditions are used at the axial boundaries and at the pinch axis with free flow conditions at the outer radial boundary. The thermal and magnetic field diffusion equations are backwards differenced and solved implicitly by quin-diagonal matrix solution using the incomplete Cholesky conjugate gradient (ICCG) iterative method of Kershaw (1978). The model is two temperature, with separate electron and ion energy equations coupled by an equilibration term. A simple optically thin radiation loss model (Post *et al.*, 1977; Tarter, 1977) is modified to include a probability of escape which allows a smooth transition to blackbody emission in the core and the adjacent plasma.

Material with a mass density below 10^{-4} kg m^{-3} is labeled vacuum and given artificially high resistivity and thermal conductivity in order to ensure that this region remains current free and isothermal. As with all other free parameters in the model, the choice of vacuum cut-off density was arrived at by trial and error, running the code many times and reducing the value until no further change in results (primarily the evolution of radius and wavelength) was observed.

The choice of such a low cut-off density allows unphysical conditions to arise where the electron drift velocity greatly exceeds the local ion sound speed. Under such conditions lower hybrid micro-instabilities grow rapidly and saturate, resulting in an anomalously high electron–ion collision frequency. The inclusion of an anomalous component to the electron–ion collision frequency in the evaluation of electrical resistivity and electron thermal conductivity serves to limit the electron drift velocity to less than the ion sound speed. It provides a physically justifiable scaling from finite plasma resistivity to virtually infinite vacuum resistivity and prevents a large discontinuity in transport coefficients at the vacuum/plasma boundary (Chittenden, 1995). While the inclusion of anomalous resistivity due to the lower hybrid drift micro-instability does affect the expansion rate

https://doi.org/10.1017/S0263034601193031 Published online by Cambridge University Press

and instability growth in the lowest density regions of the corona, it does not have as strong an effect in this work as in other work (Chittenden, 1995; Chittenden *et al.*, 1997*b*).

The results presented here use grids with 150 axial cells each 30-μm long, that is, with a grid length of 4.5 mm. These sizes were arrived at empirically by running the code exhaustively for a large number of different conditions and reducing the axial cell length and increasing the number of axial cells until no further change in results was observed. The results detailed below exhibit minimum wavelengths of 150–250 μm, indicating that 5–8 cells per wavelength are required for complete resolution. The longest wavelengths modeled below are $\sim$2 mm. The grid length of 4.5 mm thus includes a safety margin that allows the simulation to grow longer wavelengths if required.

The radial extent of the cells is set to 1.25 μm near the axis to allow the solid wire to be resolved. The radial cell extent increases with increasing radius, becoming 30-μm square at 250 μm. The long aspect ratio of cells near the axis suggests that advection of material in diagonal directions across such cells will be inaccurate. However this does not appear to affect the growth of the instability that occurs almost entirely out in the corona where the cells are square. To minimize run time for the calculations, the number of radial cells is increased or decreased so that the boundary of the problem is always 10 cells away from the largest vacuum/plasma boundary radius.

Instability growth is seeded with a $\pm$0.1% random density perturbation. Since the instability rapidly enters a nonlinear stage of development, the results after the first 15 ns are insensitive to the perturbation amplitude.

2.3. Example results in 1-D (*r*) and 2-D (*r*–*z*)

As an example, we consider a single, 15-μm-diameter aluminum wire driven by the IMP generator (150 kA, 480 kV, 65-ns 10–90% current rise time) at Imperial College. With an average dI/dt of 2×10^{12} As^{-1}, this current is comparable to the current per wire in array implosions on the SATURN and Z generators.

During the first 3.5 ns, the wire temperature gradually increases up to roughly the vaporization temperature. During this period the total pressure in the wire material is negligible and therefore the material remains stationary. Once the temperature is sufficient for the pressure to be finite and positive, the wire material begins to expand. Ionization first occurs in the lowest density surface regions forming the plasma corona.

Figure 3a shows the radial profiles after 10 ns, from 1-D (radial) simulations. The two component structure of a hot, low-density corona surrounding a cold, high-density core is already well established. Initially the core expands at roughly the sound speed of aluminum at its vaporization temperature and therefore, by 10 ns, the core has expanded threefold and its density has dropped by an order of magnitude from solid density. The expansion also cools the electrons and ions back down to roughly room temperature, which means that the pressure drops to much less than the perfect gas value, thereby reducing the rate of core expansion and keeping it intact. Despite the low temperature, the density in the core is sufficiently high for the material to have a large population of free electrons and therefore the resistivity is low and the current density is high. However, the small cross-sectional area of the core compared to that of the corona, means that only 1.5% of the total current flows in the core. Since the corona represents less than 1% of the mass of the wire during this phase, the presence of such a large fraction of the current rapidly heats the surface plasma to $\sim$50 eV. As a result, the phase transition to vapor and the first formation of surface plasma which occurs at 3.5 ns is followed by unconfined, ballistic expansion of the surface plasma at the sound speed ($\sim 5 \times 10^4$ ms^{-1} for aluminum at 50 eV). At 10 ns, the magnetic field becomes sufficient to confine the coronal plasma, and rapid expansion ceases and self-pinching begins.

Figure 3b shows the radial structure just after self-pinching at 25 ns. The corona has been compressed onto the surface of the core. Now 6% of the current is flowing in the core which is sufficient to ohmically heat the core material to $\sim$2 eV. As the core temperature rises, so does its resistivity and therefore the ohmic heating rate escalates. The core continues to expand at roughly the sound speed (at this point $\sim$2500 ms^{-1} for ionization level $\sim$1 and T_e $\sim$2 eV). The density has dropped and the temperature increased sufficiently for the pressure to be close to the perfect gas value throughout the pinch (see Fig. 2). Figure 3c shows the structure after 40 ns, the core temperature and ionization level continue to increase slowly as a result of ohmic heating. The core continues to expand, decelerating slowly in the presence of a negative pressure gradient. The corona retains the majority of current and in this one-dimensional result, remains compressed onto the surface of the core. While the condensed phases of core behavior are long gone by this time, the majority of the mass (80% lies within 100 μm of the axis) remains in a cold, dense object which is held in check by the higher pressure of the much hotter and more ionized corona.

In two-dimensional (*r*–*z*) simulations and single wire *z*-pinch experiments, the presence of $m = 0$ MHD instabilities results in substantial degradation of plasma confinement compared to Figure 3c. During self-pinching, the Alfvén transit time across the corona drops from $\sim$50 ns at 10 ns to $\sim$5 ns at 20 ns. We would therefore expect self-pinching to trigger rapid instability growth with the radial structure illustrated in Figure 3c being representative only of the neck regions of the instability.

Figure 4 shows a series of mass density maps from a 2-D simulation of one, 15-μm-diameter aluminum wire on the IMP generator. $M = 0$ instabilities are evident from $\sim$15 ns onwards, initially with $\sim$300-μm wavelength, evolving to longer wavelengths as the plasma expands, so that the wavelength divided by the radial scale length remains approximately constant. Rather than following a contorted path in

https://doi.org/10.1017/S0263034601193031 Published online by Cambridge University Press

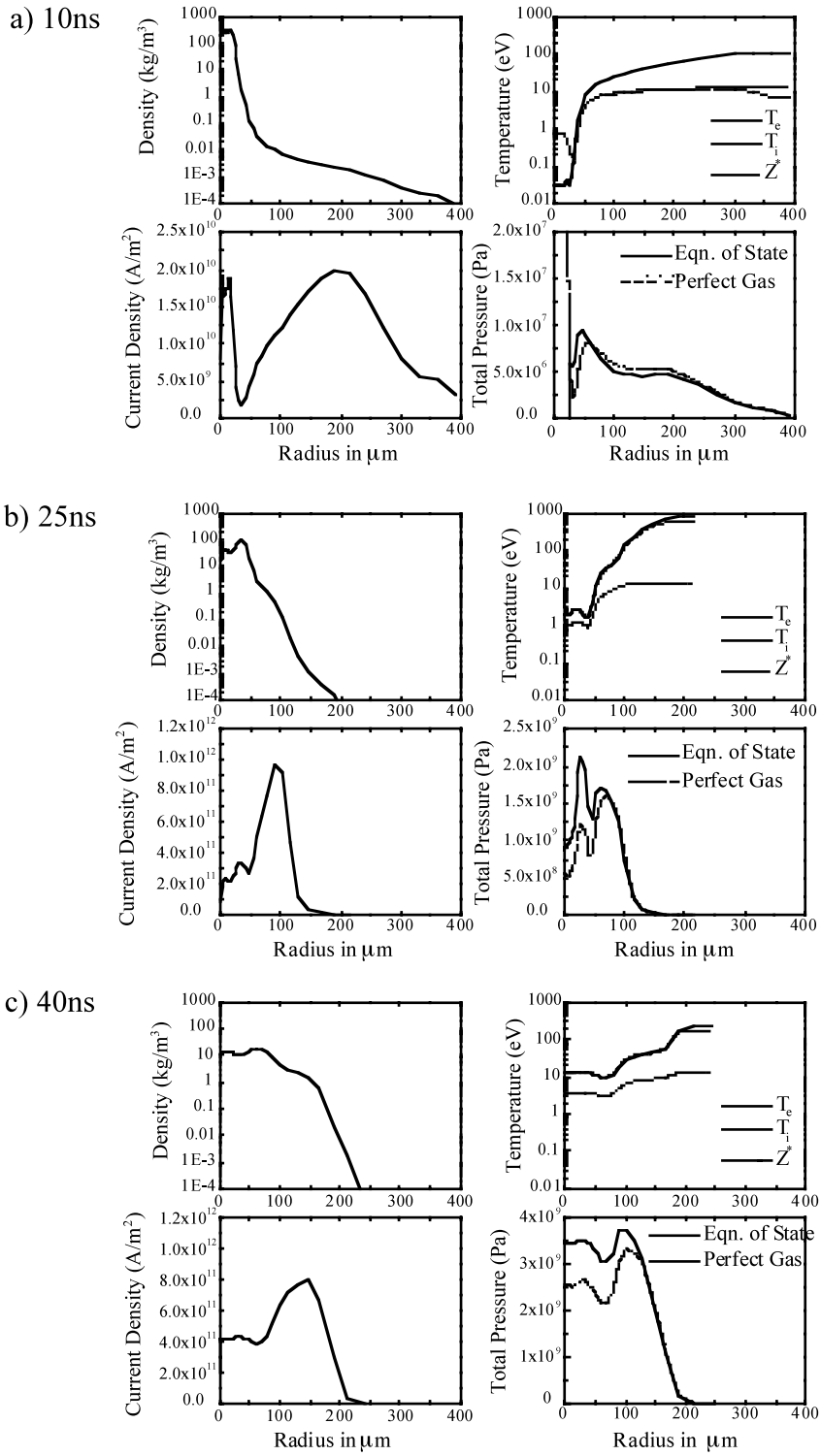

Fig. 3. Radial profiles from a 1-D (r) simulation of a 15-μm-diameter aluminum wire on the IMP generator at (a) 10 ns, (b) 25 ns, and (c) 40 ns.

and out of the radial "flares" or "bulges" of the instability, the current prefers to flow in the first available straight-line path, that is, just outside the core. As a consequence the flares of the instability are force free and almost completely unconfined and continuously expand at roughly the sound speed. Initially the "necks" of the instability fail to penetrate the core that remains almost unperturbed. Some necks apparently "bifurcate" (as described in Chittenden *et al.*, 1997*a*, 1997*b*) into two separate necks moving away from each other in the axial direction. During the first 40 ns, despite the instability, the structure remains consistent with the one-dimensional results described above. The majority of the low-density corona remains at 10–100 eV with the much higher density and lower temperature core remaining intact

https://doi.org/10.1017/S0263034601193031 Published online by Cambridge University Press

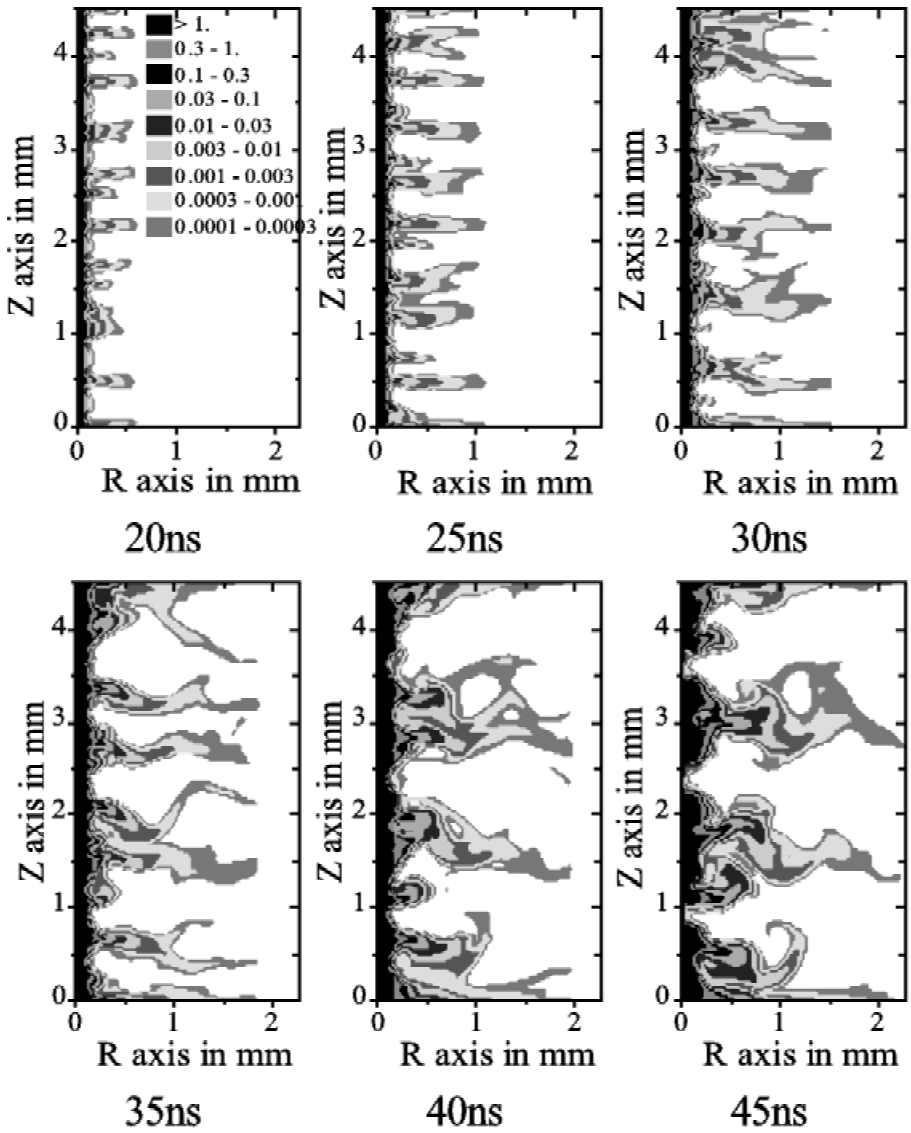

Fig. 4. A series of mass density contour maps from a 2-D (r–z) simulation of a 15-μm-diameter aluminum wire on the IMP generator.

and expanding slowly. At 45 ns the first penetration of an $m = 0$ neck into the core occurs. Since the current is now constricted to flow in a very narrow region near the axis, the electron temperature in this neck reaches several hundred electron volts. The action of the $m = 0$ instability, therefore, serves to bring the current and, hence, the high temperatures from the low-density coronal region down to the high density core, resulting in a small ($\sim$100 μm) region that is simultaneously hot and dense and which is therefore an intense source of soft X rays. Experimental observations suggest that the bright spots observed in X-ray streak photographs are coincident with the penetration of the core by the necks of the instability observed in laser schlieren photographs (Ruiz-Camacho *et al.*, 1999). Despite the penetration of the core by the neck, the vast majority of the length of the core remains intact.

The very high Alfvén and sound speeds in the neck regions and the large extent of the computational grid caused by coronal expansion made the simulation of the late time behavior of the experiment computationally prohibitive. This simulation was therefore terminated after 50 ns.

2.4. Bench testing against single wire experiments

Comparisons between simulation and experimental data for a variety of different experimental conditions provide a mechanism for testing and verifying the computational model and the cold-start theoretical algorithms contained therein. This process is facilitated by postprocessing the simulation results to generate "artificial" diagnostic images that can be compared directly with the experimental data.

Figure 5a shows a comparison of experimental and simulated laser schlieren images for a 15-μm-diameter aluminum wire on the IMP generator at 36 ns (Ruiz-Camacho *et al.*, 1999). Only light with refraction angles between 1.3 mrad and 45 mrad (determined by the size of a circular

https://doi.org/10.1017/S0263034601193031 Published online by Cambridge University Press

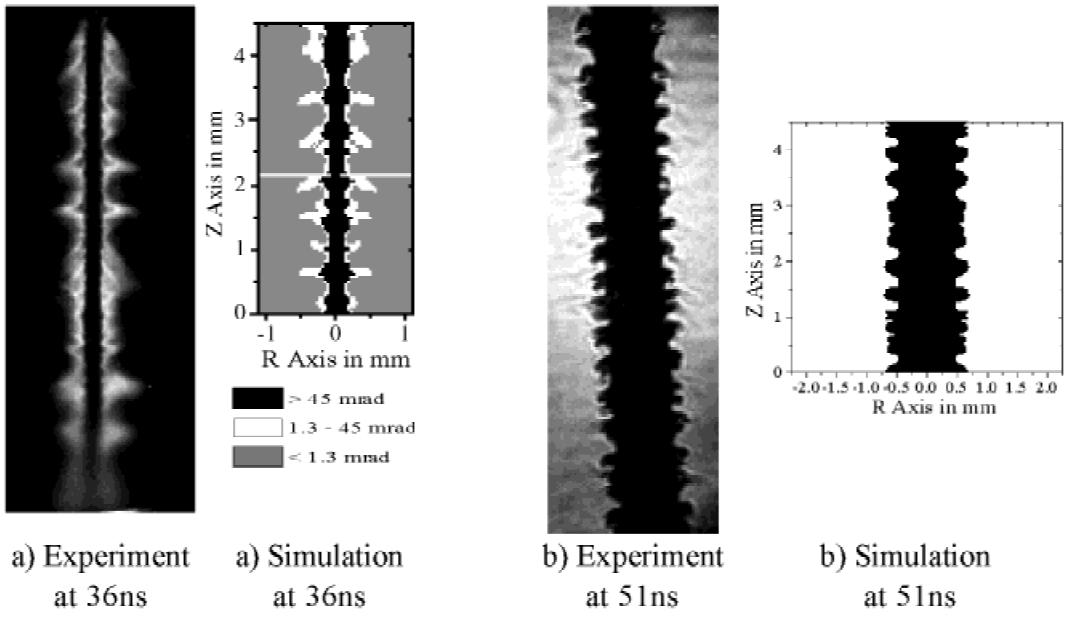

Fig. 5. Experimental and simulated laser Schlieren images for (a) a 15-μm-diameter aluminum wire on the IMP generator, and (b) a 100-μm-diameter aluminum wire on the Cornell generator.

stop and the diagnostic aperture, respectively) reaches the detector, thus providing two diagnostic cut-off contours, one in the low-density corona and one in the high-density plasma adjacent to the core. Using a similar method to Chittenden *et al.* (1997*b*), a contour map of deviation angles was constructed from the simulation data by integrating the perpendicular gradients in the refractive index along all chords crossing the two-dimensional grid. A visual comparison of experimental and simulated images shows good agreement at early times. More quantitatively, the corona minimum and maximum radii and the instability wavelengths agree to within 20% throughout the first 50 ns. The expansion of the core is, however, noticeably faster in simulation than in experiment. In addition (and probably as a consequence of this expansion), the core exhibits a greater susceptibility to penetration by the instability in simulation and therefore the late time agreement between simulation and experiment is not as good as at early times.

Similarly, Figure 5b shows a comparison of experimental and simulated schlieren data for a 100-μm-diameter aluminum-wire *z* pinch driven by a 100-ns, 145-kA current pulse at Cornell University (Kalantar and Hammer, 1993). In this schlieren system, a pinhole obscured all laser light with a deviation angle greater than ~10 mrad providing a single cut-off contour in the higher density regions of the corona. Here, the visual comparison between experiment and simulation is, if anything, better than that seen for Figure 5a. This is probably because of the large wire size, which means that the $m = 0$ instability does not begin to imprint on the wire core until ~70 ns and does not penetrate through the core at all during the current rise time. These experiments were also diagnosed using soft X-ray radiation from an *x* pinch to back-light the *z* pinch, producing absorption radiographs of the higher density regions of the core plasma. The combination of laser and soft X-ray back-lit images therefore tests the simulation's ability to reproduce the behavior of both core and coronal plasma simultaneously for the same experiment. Figure 6 shows a comparison of the experimental core and corona expansion velocities with points taken from the simulated diagnostic images. For each simulated diagnostic, a minimum and maximum radius is shown corresponding to the necks and bulges of the $m = 0$ instability. In contrast to the Imperial College experiments described above, the delay in the expansion of both the corona and core is the time taken to heat this massive wire to the vaporization temperature.

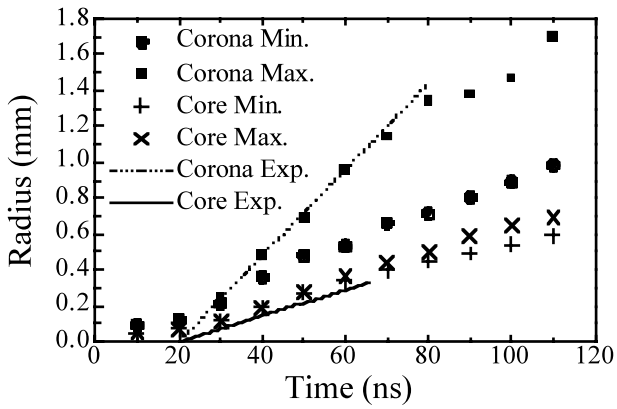

Fig. 6. Comparison of experimental and simulated core and corona expansion velocities for a 100-μm-diameter aluminum wire on the Cornell generator.

https://doi.org/10.1017/S0263034601193031 Published online by Cambridge University Press

2.5. Predictions for a single wire in an array

Figure 7 shows mass density contour maps for single wires with the same current per wire as a number of different wire array experiments (16 15-μm-diameter aluminum wires on MAGPIE, 24 25-μm-diameter aluminum wires on SATURN, 64 15-μm-diameter aluminum wires on SATURN, and 240 7.5-μm-diameter tungsten wires on "Z"). In each case, the results are plotted at the beginning of the implosion phase at a time when the equation of motion for the array suggests that the wires have moved 5% from their original radial position (8 mm for MAGPIE, 8.6 mm for SATURN, and 20 mm for Z). In each case in Figure 7, a dense wire core retains the majority of the mass within a few hundred microns of the axis and persists at least up until the time at which global implosion would start. In the case of 24 25-μm-diameter aluminum wires on the SATURN generator, in which the current per wire is by far the largest, the $m = 0$ instability development in the corona is sufficient to penetrate the core (see below). In the three other cases, the dense core and hence the majority of the mass remain unperturbed at this time.

Ideally we would wish to use this data to construct the perturbation which needs to be applied to 2-D (r–z) simulations of the final implosion phase (see Section 5). However, a quick comparison between Figure 7a and the experimental data for MAGPIE implosions (see Lebedev *et al.*, 2001, in this special issue) reveals significant differences between the 3-D behavior of wires in an array and the 2-D single wire behavior. In simulation, the average wavelength of the instability increases continuously as the corona expands (as in Section 2.3) reaching several millimeters at the beginning of the implosion. In wire array experiments, coronal plasma liberated from the wire cores is accelerated towards the common axis in the form of radial plasma streams. The plasma cross section around each wire is highly noncircular with the effective "radius" having a different evolution to that of a single wire. The instability exhibits an almost constant ~0.5-mm wavelength from early times right up until final implosion. The structure of this 0.5-mm mode is highly periodic, implying a much narrower spectrum of wavelengths than in single wires *z* pinches. There is, therefore, a clear need for 3-D cold-start calculations of single wires, and applications of these 2-D simulations to modeling wire array *z*-pinch experiments are limited to establishing trends in behavior as functions of the wire material and the current per wire.

Simulations of single aluminum wires were conducted for arrays used in a wire number scan (Sanford *et al.*, 1999) on the SATURN generator (16 30-μm-; 24 25-μm-; 32 20-μm-; 64 15-μm-; and 136 10-μm-diameter wires). These experiments showed a sharp transition in the dependence of X-ray power upon wire number at around 40 wires (corresponding to a 1.4-mm interwire gap for an 8.6-mm-radius array). While the total mass of the arrays was held roughly constant, the current per wire varied by a factor of 8.5. The results show that the amount of core material transferred to the corona and the corona expansion velocity were both weak functions of the number of wires. As a result, with fewer wires, the higher current per wire results in higher temperatures, sound speeds, and Alfvén velocities in the corona. Therefore, with fewer wires, the $m = 0$ activity is higher and the instability reaches sufficient nonlinear development for penetration of the wire core to occur prior to implosion (compare Fig. 7b and Fig. 7c). Since at the start of implosion the vast majority of the mass remains in the wire cores, there is a substantial difference in $m = 0$ perturbation amplitude between cases where the instability occurs in the corona only compared to cases where the instability penetrates the core. Consequently, one would expect lower seed levels for the magneto-Rayleigh–Taylor instability and hence shorter X-ray pulse rise times and higher X-ray powers for

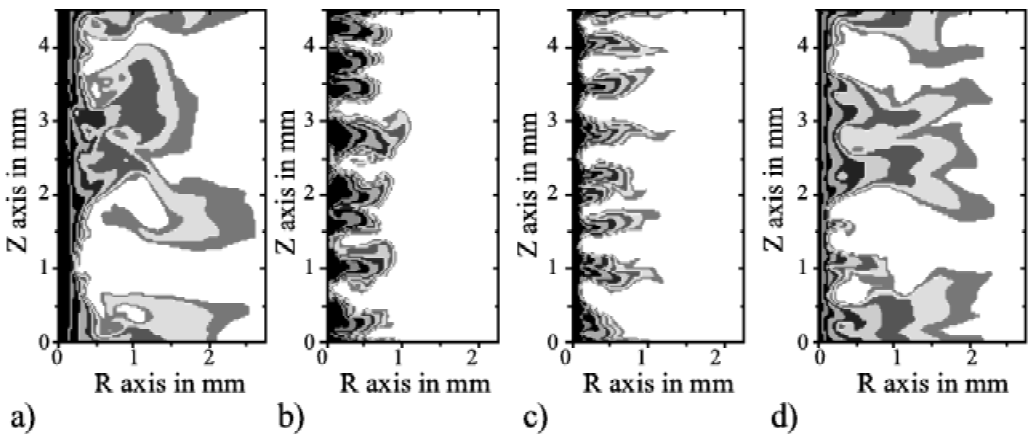

Fig. 7. Mass density contour maps (contours as in Fig. 5) for (a) 16 15-μm-diameter aluminum wires on MAGPIE, (b) 24 25-μm-diameter aluminum wires on SATURN, (c) 64 15-μm-diameter aluminum wires on SATURN, and (d) 240 7.5-μm-diameter tungsten wires on Z.

https://doi.org/10.1017/S0263034601193031 Published online by Cambridge University Press

larger numbers of wires. In simulation, the transition in perturbation amplitude occurs for this wire number scan between 32 and 48 wires, which is coincident with the experimentally observed transition in X-ray power at ~40 wires for 8.6-mm-radius arrays (Sanford *et al.*, 1996, 1999). The simulation results also indicate a general trend towards increasing plasma merger in the interwire gap and therefore increasing azimuthal uniformity with increasing numbers of wires. For example, for the 24- and 64-wire cases illustrated in Figure 7b and Figure 7c, the mass per unit azimuthal length at the midpoint between the wires and at the start of implosion, is 3% and 10%, respectively, of the average value one would obtain for a homogeneous plasma shell. The degree of plasma merger for 64 wires and above may be sufficient to reduce mass injection in the plasma formation phase and therefore results in the final implosion structure approaching that of a plasma shell.

It is interesting to note that in the simulation of a tungsten wire in an array on the Z generator (illustrated in Fig. 7d), despite substantial $m = 0$ activity in the corona, the core has not been penetrated. The core diameter, however, is ~150 μm and remains much less than the interwire gap (524 μm for a 40-mm-diameter array). The mass per unit azimuthal length at the midway point between the wires is 1.7% of the average. Thus, while the wire number is sufficiently high to effectively reduce the MRT seed perturbation amplitude, it is not sufficient to eliminate mass injection in the r–θ plane and therefore this may well contribute to the X-ray pulse broadening mechanism in these experiments (see Section 5.1).

3. MODELING THE DYNAMICS OF IMPLOSION IN THE 2-D (r–θ) PLANE

The earliest stages of plasma formation in wires in an array are the same as for single wires of the same current per wire. Once the wire cores vaporize, the material pressure greatly exceeds the effective magnetic pressure and each wire undergoes rapid cylindrical expansion, regardless of the shape of the magnetic field. Self-pinching of the coronal plasma onto the wire core introduces asymmetry not only in the r–z plane through the $m = 0$ instability but also in the r–θ plane as a result of the tear-drop shape of the total magnetic field. The initial expansion of wire core means that much of the complex physics associated with the very high densities of the "cold-start" phase (such as the modifications to the equations of state) become redundant and can be dropped. It therefore makes sense to use 1-D (r) or 2-D (r–z) cold-start simulations of individual wires up until the start of self-pinching and then to use the results of these simulations to provide the initial conditions for 3-D simulations based on the perfect gas equation of state. As shown in Section 1.2, the 3-D results obtained to date have been limited to low resolution. In this section we analyze the effects of azimuthal asymmetry in 2-D (r–θ) or 2-D (x–y) coordinates.

3.1. Description of the 3-D resistive MHD code

The 3-D resistive magneto-hydrodynamic (MHD) code (Chittenden *et al.*, 1999) has been developed specifically to model wire array z-pinch experiments. The code performs explicit hydrodynamics on a Cartesian (x-y-z) Eulerian grid with cubic cells, using second order Van-Leer advection. The thermal and magnetic field diffusion equations are solved implicitly by iterative solution of matrix equations. In the case of the magnetic field diffusion, the three magnetic field components (located on the cell face centers) are diffused simultaneously using an algorithm that conserves $\nabla \cdot \mathbf{B}$. This results in a matrix equation with a $3n \times 3n$ matrix (where $n = n_x n_y n_z$ is the total number of cells) containing 29 nonzero diagonals. Solution of this matrix equation typically consumes 90% of the run time. The model is two temperature (electrons and ions) with local thermodynamic equilibrium (LTE) ionization and a simple radiation loss model (Tarter, 1977). Three-dimensional runs of the full array with adequate spatial resolution would require unrealistic computational run times. Three-dimensional simulations of a single wire in an array are presently under development. The data from this code presented here concentrate upon adequately resolved two-dimensional results in the x–y (or r–θ) plane.

In order to avoid the need for extremely fine scale spatial resolution at early times, a 1-D (r) cold-start simulation (see Section 2) of the first few nanoseconds is run to provide the initial conditions for the 2-D (x–y) code. Typically, the cold-start calculation is run up until the start of the self-pinch of the corona. The rapid expansion prior to this point is insensitive to the shape of the magnetic field and it is only when the magnetic field becomes large enough to pinch the plasma that its shape in the x–y plane becomes important. By this stage, the expansion of the core is generally sufficient for moderate (30–100 μm) cell sizes to be sufficient and for a perfect gas treatment of the equation of state to be adequate.

3.2. Results for low wire numbers

Figure 8 shows a progression of logarithmic mass density contours from a 2-D (x–y) simulation of a 16-mm-diameter array of eight 15-μm-diameter aluminum wires driven by the MAGPIE generator. One quarter of the full array is simulated with reflective boundary conditions. At 60 ns, the coronal plasma has been significantly deformed by the global magnetic field of the array. The absence of current in the neutral wire cores and their high mass density mean that up until ~80% of the final implosion time they remain virtually unmoved. However, any further material, liberated from the wire cores into the low-density corona, experiences rapid acceleration by the $\mathbf{J} \times \mathbf{B}_{global}$ force towards the array axis. As a consequence, the plasma coronas are swept around the wire cores giving rise to radial streams of plasma. The rate at which material is ejected from the dense wire core into the low-density corona both controls and is determined by the rate at which this material is removed from around the core

https://doi.org/10.1017/S0263034601193031 Published online by Cambridge University Press

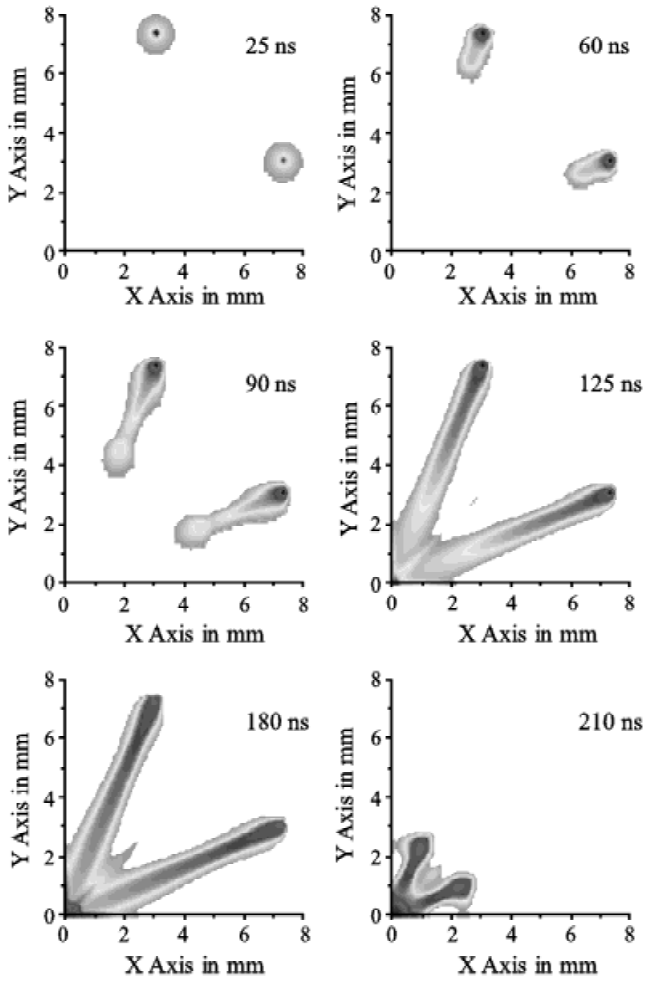

Fig. 8. A progression of mass density contours from a 2-D (x–y) simulation of 8 15-μm-diameter aluminum wires on MAGPIE. Contour levels are as in Figure 13.

and injected into the array's interior. There therefore exists a dynamical balance between these two processes which control the rate of wire core ablation and therefore the implosion dynamics of the array.

The plasma in the streams is kept cool, primarily by ionization energy losses and to a lesser extent by radiative cooling, and maintains roughly constant 10- to 20-eV electron and ion temperatures. The average radial velocity of plasma in the stream is $\sim 10^5$ ms^{-1}, that is, five times the local ion sound speed. Since the magnetic field is partially "frozen" into the plasma, the radial streams bring current inside the array radius. The fraction of the current inside the array is determined by a balance between current being injected with the plasma streams and diffusion of the magnetic field that returns this current to flow in the lowest inductance path adjacent to the wire cores. This effect is dependent on the Lunqvist number (or magnetic Reynold's number) of the plasma streams. Penetration of the current inside the array is reduced in calculations with more wires and hence smaller interwire gaps and better screening. As an example, 41% of the current flows within 6 mm of the axis for 8 wires at 125 ns, this figure drops to 32% for 16 wires and 24% for 32 wires.

The radial streams of plasma first interact with one another at 105 ns at a radius of 2.5 mm. Ten nanoseconds later, at roughly half the final implosion time, the first plasma arrives on the axis. The density contour map at 125 ns illustrates the structure of the "precursor" pinch formed on axis (see Section 3.3). Low density material pervades the region within the interaction radius; however this material retains its radial velocity and converges to the axis to form a high-density, high-temperature central region of $\sim$500-μm diameter.

From this point onwards, the implosion of the array is a continuous process. The wire cores are gradually depleted as they ablate more coronal material that is rapidly accelerated towards the accreting precursor plasma on axis. Figure 9 shows the fractions of mass in the wire cores and in the precursor on axis as functions of time. The gradual increase in precursor mass is accompanied by an increase in current transferred to the precursor. However, it is the inertia of the radial plasma streams which confines the precursor and maintains a roughly constant 40-eV temperature rather than magnetic confinement and ohmic heating, since less than 10% of the total current is transferred. With higher numbers of wires, the current transferred to the precursor becomes negligible.

By 175 ns, the wire cores have fully ablated, generating a high-density plasma from 6- to 8-mm radius containing 40% of the array mass. The final implosion of this mass is very rapid and generates the substantial kinetic energy that is responsible for X-ray production at the final stagnation.

The mass density contour map at 210 ns shows the pinch structure just prior to final stagnation. In cylindrical shell implosions (in the absence of instabilities) one would expect 100% of the mass to reach the axis almost simultaneously with a final collapse velocity of $\sim 3 \times 10^5$ ms^{-1}. By contrast, the final collapse stage of an 8-wire array is comprised of

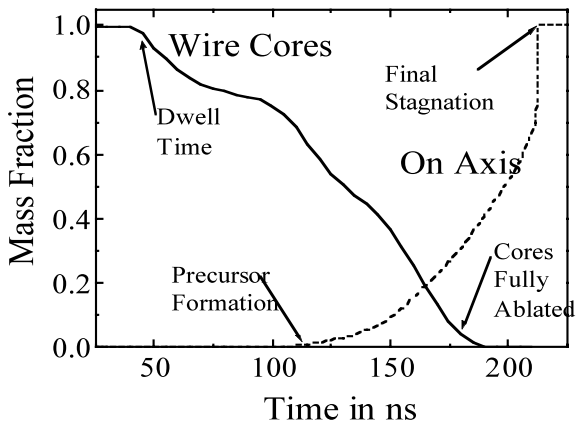

Fig. 9. The fraction of mass in the wire cores and precursor as functions of time for 8 15-μm-diameter aluminum wires on MAGPIE.

https://doi.org/10.1017/S0263034601193031 Published online by Cambridge University Press

azimuthally discrete radial plasma streams containing 40% of the mass impacting at 4.5×10^5 ms^{-1} onto a precursor containing 60% of the mass. The reduced mass and increased velocity of the final implosion result in similar kinetic energy and X-ray yield to that of a cylindrical shell. The fact that the implosion time for this distributed implosion agrees to within 5% with the time predicted by the zero-dimensional thin-shell model remains one of the most remarkable features of low wire number arrays. A clue as to why this should be comes from the fact that the mass averaged radius *versus* time, even for eight wires, agrees well with the 0-D trajectory.

Quantitative comparisons of these results with experimental data (Lebedev *et al.*, 1998*b*, 1999) indicate accurate agreement for a number of key parameters. The time of first observable expansion of the wire corona (the dwell time), the inward radial, azimuthal, and outward radial velocities, the timing of the first plasma on axis, the time of first X-ray emission from the precursor, and the time of final implosion are all in agreement to within 10%. The electron number density profiles for the plasma around the wires, in the radial streams, and in the precursor are also in close agreement.

Simulations of MAGPIE experiments with up to 32 15-μm-diameter aluminum wires exhibit qualitatively similar behavior. Despite the fact that merger of the lower density regions of the plasma streams occurs earlier with more wires, the persistence of the wire cores until late in the discharge means that azimuthal asymmetry is retained throughout the implosion. For 8, 16, and 32 15-μm-diameter aluminum wires, the wire cores always remain stationary at their original positions until ~80% of the implosion time, at which point they undergo rapid implosion. Thus the trajectories of the radius versus time (normalized to the implosion time) are almost identical for each case and are characteristic of the implosion of discrete (nonmerged) wire plasmas. Precursor plasmas always form at roughly half the final implosion time and build up a significant fraction of the array mass (50% for 32 wires) prior to final implosion. Even with 64 15-μm-diameter aluminum wires on MAGPIE, the dominant physical processes remain the same, although in this case the proximity of the wire cores results in a slightly different dynamical mode of implosion (see Section 3.4).

Qualitatively similar results have also been obtained for experiments on higher current generators with larger numbers of wires, for example, for a 17.12-mm-diameter wire array of 64 15-μm-diameter aluminum wires on SATURN (Sanford, 2001). Figure 10 shows a mass density contour map at 35 ns, shortly before ablation of the wire cores, showing the strong azimuthal modulation that is retained throughout the implosion. Precursor material is evident on axis from 30 ns onwards. The shorter time-scales of these experiments, however, mean that for 64 wires only 10% of the array mass builds up in the precursor prior to the final implosion when the remaining 90% impacts upon it. The profile of integral mass as a function of radius obtained from Figure 10 is very similar to the initial profiles used in 1-D

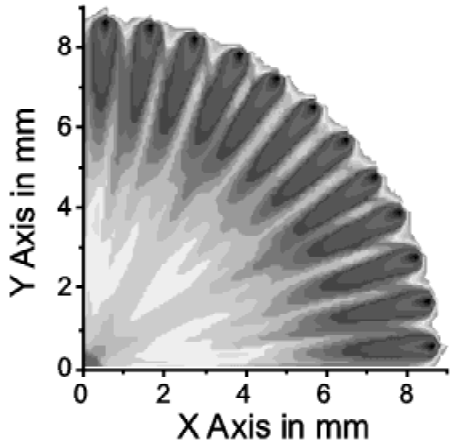

Fig. 10. A mass density contour at 35 ns from a 2-D (x–y) simulation of 64 15-μm-diameter aluminum wires on SATURN.

radiation hydrodynamics simulations (Whitney *et al.*, 1997) where the artificial introduction of precursor material was found to be necessary in order to reproduce the spectral features observed in experiments.

3.3. The physics of the precursor plasma

The most remarkable feature of precursor plasmas is their apparent uniformity, stability, and longevity as exemplified by MAGPIE experimental laser probing images and gated X-ray images (see Lebedev *et al.*, 2001). The stability is testament to the fact that the precursor is not a magnetically confined plasma. Despite large mega-ampere currents flowing through the wire array, the screening effect of the wires means that only a very small fraction of this penetrates through to the precursor. The precursor is in fact confined by the continuous bombardment of plasma from the radial streams. While the behavior of the wire plasmas remains very much three-dimensional and the radial streams of plasma are strongly modulated in both the axial and azimuthal directions, the merger of these plasma streams on their way to the axis results in a homogeneous one-dimensional convergent plasma flow onto the surface of the precursor. The radial velocity of the plasma streams observed in aluminum wire array experiments on MAGPIE of 1.5×10^5 ms^{-1} equates to a kinetic energy per ion of ~3 keV. The ρv^2 of the streams is in the range 1–10 GPa (increasing slowly in time) which balances the thermal pressure of the precursor. The kinetic energy of the bombarding plasma stream is thermalized in an energy deposition region at the surface of the stationary precursor and provides a continuous source of heat.

Increasing the number of wires in the array increases both the density and the symmetry of the bombarding plasma streams and leads to observably tighter and denser precursors. Changing the diameter of the array changes the implosion velocity and hence the kinetic energy of the plasma

https://doi.org/10.1017/S0263034601193031 Published online by Cambridge University Press

streams and the rate of precursor heating. However, it is the level of radiative cooling which dominates the energy balance in the precursor and therefore the choice of material is the most important factor in determining the temperature. It is therefore possible (within a limited range) to control the density and temperature of precursor plasmas by the choice of initial wire array parameters.

The dominance of radiation loss in the energy balance of a precursor plasma is evident from experimental data. In aluminum arrays, for example, measurement of X-ray flux from the precursor using a diamond photo-conducting detector with no filter (to register full wavelength range) implies an output of 1–10 GW rising slowly (Lebedev *et al.*, 2001). This almost exactly balances the incoming kinetic energy of the plasma streams given by $\frac{1}{2}\rho v^3 A$ (where A is the surface area of the precursor). Comparing these input and output powers with the instantaneous internal energy of the precursor (either from simulation or calculated from experimental estimates for the electron density and temperature), the characteristic heating and cooling times are in the 1- to 10-ns range. Over a 200-ns lifetime, therefore, the precursor exists in a quasi-equilibrium state with the radiation and ionization energy loss rates being roughly balanced by the incoming flux of kinetic energy. Since the radiation loss rate determines the temperature and hence the ionization level and the pressure, it also determines the density to which the precursor will be compressed by the ρv^2 of the bombarding plasma streams. In tungsten wire arrays, the increased radiation loss allows the precursor to be compressed to much smaller diameters than for aluminum.

The initial formation phase of the precursor when the first plasma arrives on the axis requires a kinetic description and cannot be modeled using the fluid codes described here. The high velocity of the plasma streams implies low collisionality and long ion mean free paths. Eventually the flux of material through axis becomes high enough for collisions to become important and for some ions to be stopped on the axis. The increase in density also increases the collision rate and hence there is a nonlinear escalation in collisionallity that allows the precursor plasma to be seeded on axis. There is therefore a delay between the first arrival of material at the axis and the formation of a dense radiating precursor. In aluminum this delay is only a few nanoseconds but for tungsten, where the kinetic energy per ion in MAGPIE experiments can exceed 20 keV, the mean free paths are longer and the delay is several tens of nanoseconds.

Once a collisional precursor plasma has been established, the behavior of the precursor observed in experiments can be approximately reproduced by the 2-D (x–y) MHD simulations described above. However, since the plasma flow close to the axis is effectively 1-D and free of magnetic field, the precursor behavior can be modeled with much higher spatial resolution using a simple 1-D hydrodynamic model. Figure 11 shows results from a 1-D Eulerian hydrodynamic simulation of the precursor in an array of 16 15-μm-diameter aluminum wires on MAGPIE,

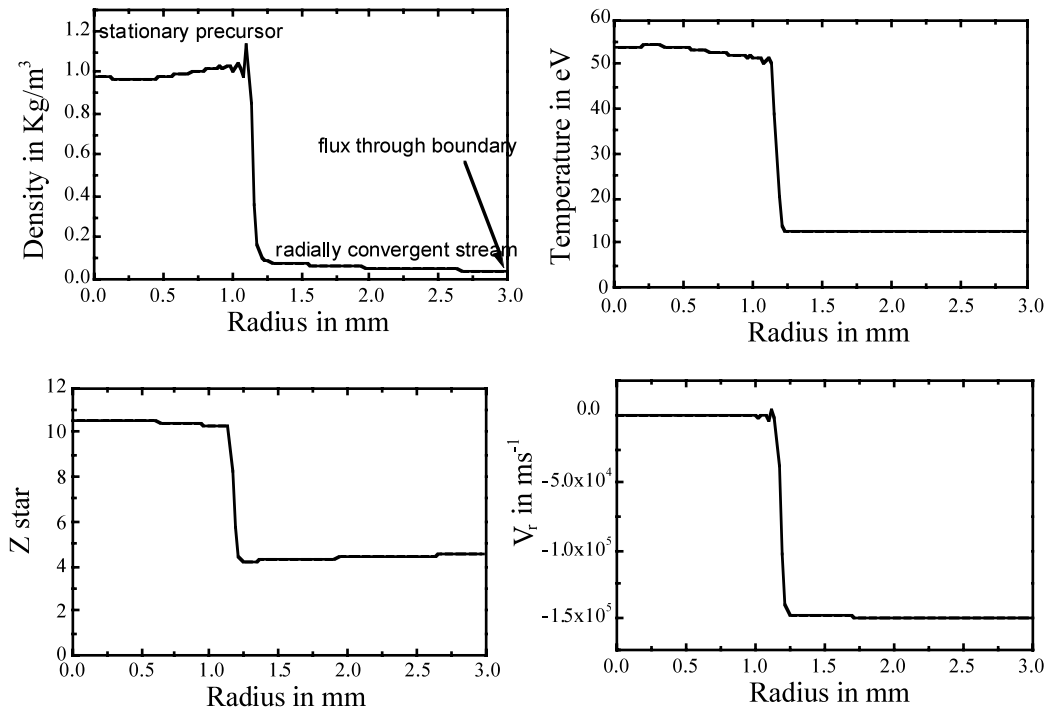

Fig. 11. Radial profiles of mass density, electron temperature, Z^*, and radial velocity from a 1-D hydrodynamic simulation of the precursor in an array of 16 15-μm-diameter aluminum wires on MAGPIE.

https://doi.org/10.1017/S0263034601193031 Published online by Cambridge University Press

which incorporates a simple radiation loss model (Tarter, 1977; Post *et al.*, 1977). A continuous flux of plasma is injected in through the right-hand boundary with radial velocity -1.5×10^5 ms^{-1}, $T_e = T_i = 20$ eV, and plasma density at $r = 3$ mm either 0.01 kg/m^3 or 0.1 kg/m^3 or linearly rising from 0.01 kg/m^3 to 0.1 kg/m^3 in 100 ns (best match to experiment). After reaching the axis, the plasma first bounces around and then converges to a two-component equilibrium with a high-density stationary precursor plasma and a lower density convergent radial plasma stream. The pressure gradient in the precursor is balanced by the ρv^2 of the bombarding stream. The kinetic energy delivered to the precursor ($\frac{1}{2}\rho v^3 A$, where A is the surface area) is roughly balanced by the radiation losses. The discontinuity between the flowing low density stream and the stationary high-density precursor represents a strong shock, and it follows from simple shock theory that the ratio between the density just outside the precursor and that inside the shock should, in cylindrical geometry, be $[(\gamma + 1)/(\gamma - 1)]$. The results suggest that for aluminum at 180 ns, the value of γ is $\sim$1.2. In experiments with tungsten arrays, however, the stream density is comparable to the aluminum case, but the precursor density is much higher. If we make the assumption that the same fraction of the mass is in the tungsten precursor as with aluminum, then since the diameter is roughly ten times smaller, the density is roughly 100 times higher, implying a γ for tungsten close to 1. Thus the highly radiative nature of the tungsten plasma makes it highly compressible and allows it to collapse under effect of radiative cooling to much higher densities than lower-Z elements. Unfortunately this hypothesis cannot be tested using the 1-D code described here, as the optically thin radiation loss model cannot treat the radiative cooling of a dense tungsten plasma properly as it requires a multigroup radiation transport model for accurate solution.

In fact this problem apparently represents an almost ideal 1-D radiation-hydrodynamics bench-test problem, with extremely simple and robust initial conditions and a single critical experimental parameter (the radius of the precursor) for comparison. This test problem is indeed very similar to a test developed to evaluate different artificial viscosity formulations in 1-D hydrodynamics (Noh, 1987). However the use of precursor plasmas goes far beyond the computational. A wide variety of potential plasma physics experiments which have to date been impossible due to the absence of a long-lived, uniform, and stable dense plasma are feasible using a precursor plasma. For example, if a titanium precursor plasma can be made with an electron temperature of 150–200 eV and an electron density around 10^{25} m^{-3}, then this represents an almost ideal medium for the collisionally pumped neon-like titanium soft X-ray laser scheme. While this X-ray laser scheme has already been demonstrated in a number of laser-produced plasma experiments, the size and duration of the precursor plasma has the potential to produce laser pulses with up to two orders of magnitude higher saturation amplitudes and pulse widths. In addition, the uniform density and temperature inside the precursor and the high contrast in density compared to the bombarding stream make it an almost ideal test plasma for absorption spectroscopy measurements of opacity and a low cost alternative to the *z*-pinch-driven hohlraum-based opacity measurements described by Springer *et al.* (1997).

3.4. Higher resolution results for high wire numbers

A reduced 2D computational zone, centered around a single wire, was adopted in order to be able to model larger diameter arrays and to use finer spatial resolution (i.e., 20-μm square cells). Reflective boundary conditions were used on the top and bottom azimuthal boundaries; however free-flow boundary conditions were used on the left- and right-hand radial boundaries, allowing material to pass through the computational zone. Since the code is Cartesian with rectangular cells in *x*–*y* coordinates, the effect of the radial convergence of the plasma flow cannot be incorporated. If, however, the radial width of the computational zone is small compared to the radius of the array, then the error introduced is minimal.

Simulations of 8–32 15-μm-diameter aluminum wires on MAGPIE again show mass injection forming radial plasma streams and resulting in the characteristic "discrete wire" implosion trajectory with the wire cores remaining stationary until 80% of the implosion time. In simulation, the implosion trajectory is monitored by tracking the position of the local density maximum near the plasma edge, which can then be compared to experimental data for the radius *versus* time measured from optical streak photographs (see Fig. 12). For 64 wires, the implosion trajectory begins to approach that of the 0-D thin shell as in experiment (Lebedev *et al.*, 2000*b*). This is because the size of the slowly expanding, dense wire core can become a significant fraction of the interwire gap prior to implosion. Therefore it becomes increasingly difficult to push the plasma and in particular

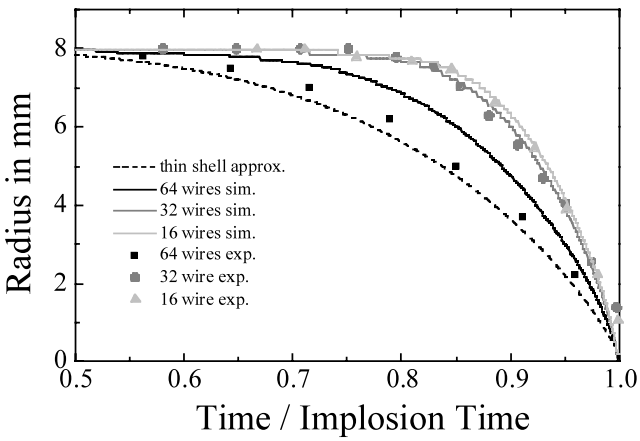

Fig. 12. Trajectory of the local density maximum near the plasma edge, compared to experimental data measured from optical streak photographs, for 16, 32, and 64 15-μm-diameter aluminum wires on MAGPIE.

https://doi.org/10.1017/S0263034601193031 Published online by Cambridge University Press

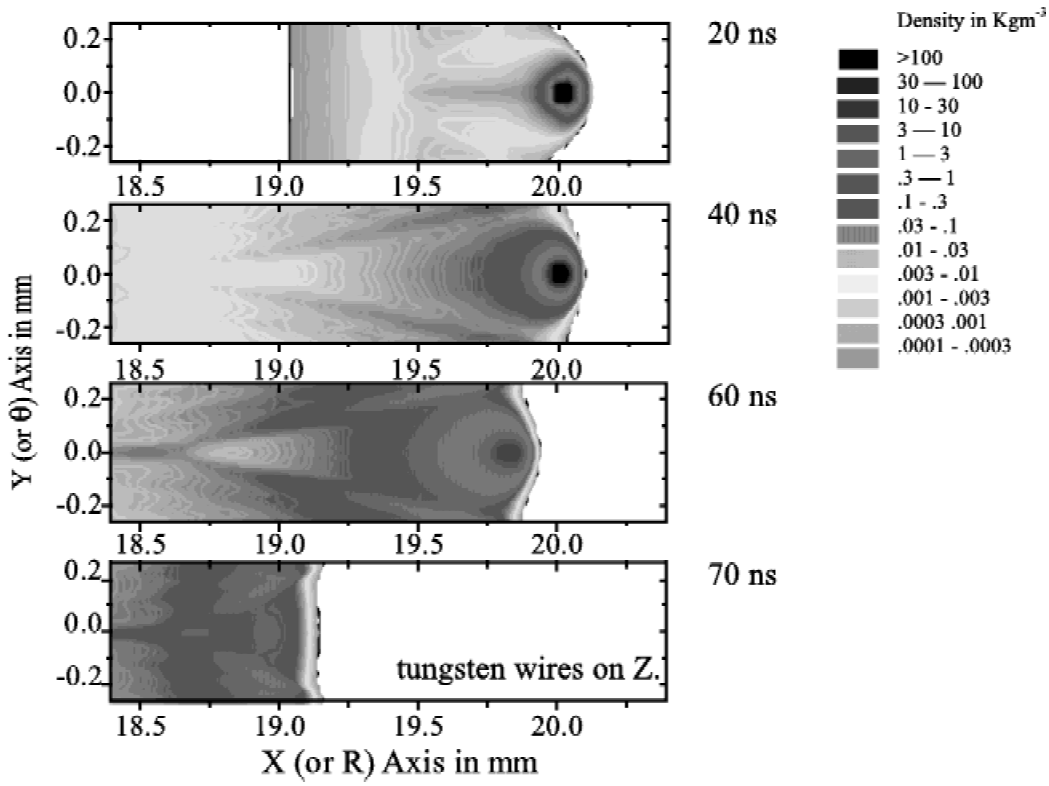

Fig. 13. A progression of mass density contours from a 2-D (*x*–*y*) simulation of 240 7.5-μm-diameter tungsten wires on Z.

the magnetic field through the decreasing gaps between the cores, and the mass injection process is reduced. The array then adopts a more azimuthally symmetric implosion.

Mass density contour maps for a 40-mm-diameter array of 240 7.5-μm-diameter tungsten wires on the Z generator (see Fig. 13) exhibit many of the features synonymous with lower wire number experiments (Lebedev *et al.*, 1998*b*, 1999; Chittenden *et al.*, 1999). Again, the structure of the imploding plasma is determined by the persistence of dense, cold, and predominantly neutral wire cores that retain a large fraction of the mass. The high density of material in the wire cores and the low level of current flowing in them means that they remain stationary. The $\mathbf{J} \times \mathbf{B}$ force acts solely on the low-density plasma coronas, pushing this material through the gaps between the wire cores and injecting it into the interior of the array in the form of radial plasma streams. Merger of low-density plasma from adjacent wires in the interwire gap occurs early on; however the density of this material is too low to prevent it from being swept inside the array.

From the flux of material leaving the computational grid through the left-hand boundary, we can construct a radial profile of mass density for the ensuing implosion (see Fig. 14). At 75 ns, the radial plasma stream extends down to 6-mm radius and contains ~20% of the array's mass with the remaining 80% in a 2-mm-wide shell. During the final implosion, the outer shell is accelerated to a much higher velocity than the velocity of mass injection that occurred earlier. Therefore, for a single array with these parameters, the majority of the mass injected is caught and snow-ploughed up by the main implosion before reaching the axis, and the precursor plasma formed on the axis by the radial plasma stream exists for only ~10 ns prior to the main implosion. In single arrays with fewer wires, however, a larger fraction of mass is injected between the wires so that the radial profile of mass at the start of implosion is dependent on the number of wires. The azimuthal symmetry of the plasma flux leaving the computational zone in Figure 13

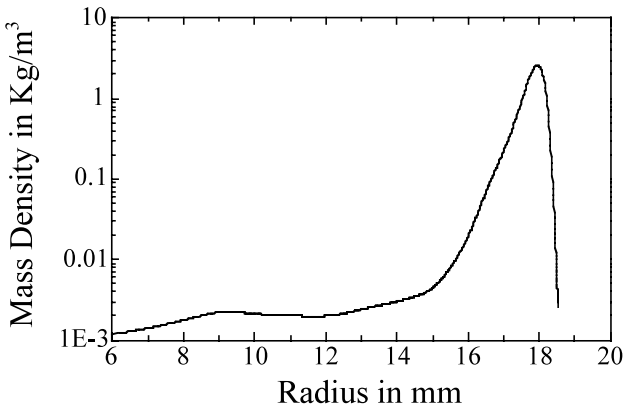

Fig. 14. Radial profile of mass density for 240 7.5-μm-diameter tungsten wires on Z at 75 ns.

https://doi.org/10.1017/S0263034601193031 Published online by Cambridge University Press

suggests that, provided the correct radial profile and axial perturbation are used, 2-D (r–z) simulations of the final stages of implosion are adequate for single arrays.

4. MODELING NESTED WIRE ARRAYS IN THE 2-D (r–θ) PLANE

4.1. The different modes of interaction between nested wire arrays

The first interpretations of the benefits of nested wire arrays were based on the assumptions that both arrays form annular plasma shells and that the Rayleigh–Taylor (RT) instability that develops in the outer array is essentially annihilated during collision with the inner array (Deeney *et al.*, 1998). In this "hydrodynamic collision" mode, the final implosion of the combined masses then occurs very rapidly with little time for instability development (see Fig. 15a). However, the electrical screening effect of large numbers of exploded wires in the outer array reduces the current in the inner to a few percent, or less, of the total and therefore significant early expansion of the inner array wires seems unlikely. The other extreme is that the inner array wires remain discrete until the outer array material has passed through their gaps. The full current is then transferred rapidly to what was initially the inner, imploding it rapidly onto the outer array material on axis (Davis *et al.*, 1997; Terry *et al.*, 1999). In this "transparent inner" mode the benefit again comes from reduced RT growth compared to a single array since the final implosion of the inner array occurs very rapidly once the maximum generator current is rapidly transferred to it (see Fig. 15b). This implosion mode has recently been observed in nested wire array experiments on the MAGPIE generator at Imperial College (Lebedev *et al.*, 2000*a*). A third possibility is that the small current flowing initially in the inner array generates a small seed magnetic flux between the arrays which is compressed by the imploding outer array. As the outer array approaches the inner, the amplitude of the compressed flux becomes large enough to push the inner array towards the axis ahead of the outer. Thus a magnetic flux buffer prevents collision of the two arrays until both reach the axis almost simultaneously. Despite the fact that the optimal wire array parameters for each mode are different, there is as yet no conclusive evidence as to which nested mode is in operation in experiments on Z.

To try and establish which mode is likely, we model the bombardment of inner array wires by the stream of plasma coming from the outer array. From the results of Section 3.4, we obtain the average flux of plasma density, momentum, energy, and magnetic field through the left-hand boundary of a computational box simulating the outer array of a nested configuration. These fluxes (modified for convergence) are then used as boundary conditions on the right-hand boundary of a similar computational box for the inner array. In this simulation, the hydrodynamic routines were modified to allow independent advection of material from the two arrays, thus allowing the motion of the two arrays to be tracked independently.

4.2. Results for conditions on the Z generator

Figure 16 shows separate density contours for a stream of material from an outer array of 240 7.5-μm-diameter tungsten wires bombarding an inner array of 60 10.5-μm-diameter tungsten wires on Z. At first the low-density outer array material passes through the gaps between wires, setting up a bow shock as it streams around the inner wires. At this stage the size of the dense wire core remains a small fraction ($\sim$5%) of the interwire gap and the rate of energy and momentum transfer to the inner array wires is small. As the main implosion approaches the inner wire, the density of the bombarding material increases rapidly and the rate of kinetic energy dissipation reaches 100 GW on each wire, causing rapid heating, ablation, and expansion of the wire core. As the cross section of the wire core increases to occupy a larger fraction of the interwire gap, so the efficiency of momentum and energy transfer to the inner wires increases, which in turn causes faster heating and expansion so that the wire explosion is highly nonlinear. The core temperature goes from $\sim$2 eV to 100 eV in less than 5 ns and expands in the azimuthal direction at roughly the corresponding sound speed ($C_S \sim 5 \times 10^4$ ms^{-1}). Therefore, during the time taken

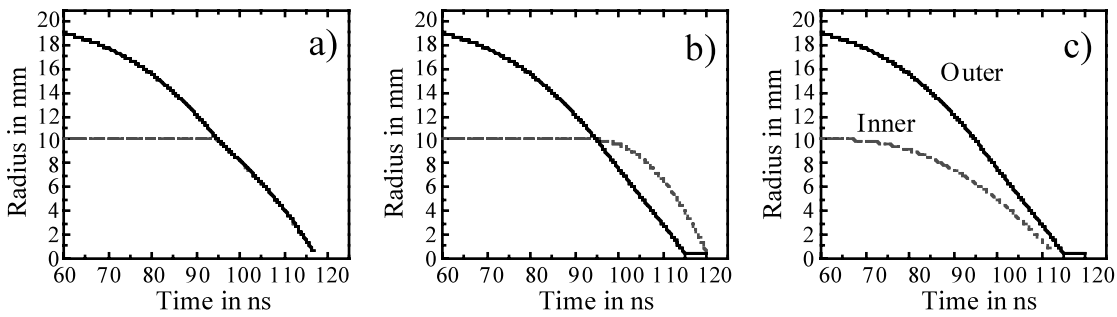

Fig. 15. Schematic showing the different trajectories of the three dynamical modes of nested array implosion, (a) hydrodynamic collision mode, (b) transparent inner mode, and (c) flux compression mode.

https://doi.org/10.1017/S0263034601193031 Published online by Cambridge University Press

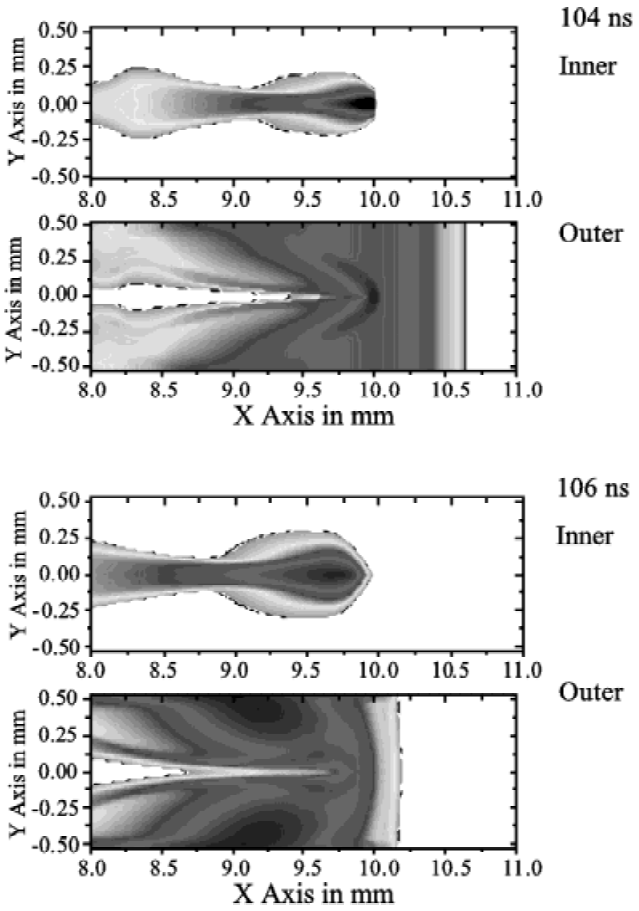

Fig. 16. Mass density contour maps from a simulation of a nested array interaction on Z.

for the main shell of outer array material to pass by the inner wires, the inner wires expand to a diameter of $2\Delta C_S/v_0 \approx$ 1 mm (i.e., roughly half the interwire gap), where here the outer shell has a velocity $v_0 = 4 \times 10^5$ ms^{-1} and a width $\Delta =$ 2 mm. At 106 ns, the majority of the outer array material has passed by the inner array wires through the interwire gaps. However the momentum transferred during collision is sufficient for the inner to have ~80% of the radial velocity of the outer and therefore the implosion trajectory is virtually indistinguishable from the hydrodynamic collision mode (see Fig. 15a). Since most of the outer material passes through the interwire gap, however, there is no strong shock as there would be between two colliding annular shells and consequently the "first-strike" radiation is much less than in the pure "hydrodynamic collision" mode modeled by 2-D (r–z) simulations (Deeney *et al.*, 1998).

The current injected between the outer array wires and carried in the stream is typically small, ~10% of the total. However as part of the plasma stream stagnates against the inner wire, the magnetic flux which it carries becomes highly compressed so that, at 104 ns, a current of several megaamperes flows in the inner array with a reversed current in between the inner wires and the outer shell. The net effect of magnetic flux compression is to provide a mechanism for increasing the level of momentum transfer during collision. Simulations with the magnetic field set to zero, that is, a purely hydrodynamic interaction, show much less momentum transfer and result in something akin to the "transparent inner" implosion mode (see Fig. 15b).

For inner arrays with the same total mass but more wires, for example, 120 7.5-μm-diameter tungsten wires, the reduced interwire gap results in almost complete coalescence of the two array materials. For fewer wires, for example, 30 15-μm-diameter tungsten wires, the interwire gap is large compared to the distance that the wire core expands during the interaction. The level of momentum transfer is therefore small, with the inner array having only 14% of the outer array velocity postcollision, and the trajectory is more like the transparent inner mode.

5. THE RAYLEIGH–TAYLOR INSTABILITY

The r–θ plane simulations described in Section 3 suggest that after the radial plasma streams have propagated for more than ~4 times the interwire gap, then the streams are highly merged and any remaining azimuthal asymmetry is negligible. For example, for 40-mm-diameter single (or outer) arrays on Z containing 240 wires, the plasma flow becomes azimuthally homogeneous inside a radius of about 18 mm. The use of 2-D (r–z) modeling of the final implosion phase in high wire number arrays would therefore appear to be justified, provided the effects of the azimuthal dimension upon the radial profiles and perturbation levels are taken into account. This is not to say that the development of the Rayleigh–Taylor in 3-D will not be different from that predicted by 2-D codes. Linear stability theory suggests (Hammer & Ryutov, 1999) and experiments show (Lebedev *et al.*, 2001) that in 3-D, even when the array wires remain discrete and are not merged, the $m = 0$, r–z plane Rayleigh–Taylor modes are dominant. However, the low-resolution simulations in Section 1.2 indicate that persistence of dense wire cores forces the spikes of the RT instability to be anchored to the original positions of the wires, implying a different behavior during implosion to that of the 2-D (r–z) modeling presented in this section.

5.1. 2D (r–z) simulations of a shell-like implosion

Following a similar method to that employed by other authors (e.g., see Peterson *et al.*, 1999; Douglas *et al.*, 2000), we model the Rayleigh–Taylor unstable implosion phase and the stagnation phase using a 2-D (r–z) resistive MHD code. The model is similar to that described in Section 2.2, but for this application uses a simple LTE-Saha ionization model, a perfect gas equation of state and Spitzer-like resistivity (incorporating the anomalous component due to lower hybrid micro-instability). The runs presented here use 100-μm-square cells and grids of axial length 10 mm, which allows the dominant wavelengths of 1–2 mm to be well

https://doi.org/10.1017/S0263034601193031 Published online by Cambridge University Press

resolved. Again these sizes were arrived at empirically by running the code exhaustively for a large number of different conditions and reducing the axial cell length and increasing the number of axial cells until no further change in results was observed.

By way of an example, Figure 17 shows a sequence of mass density contour maps from a 2-D (r–z) simulation of an aluminum plasma shell driven by the MAGPIE generator. In this case, the code was initialized using a simple 1-mm-wide uniform shell and instability growth was initiated using a cell-by-cell random density perturbation with a rather large amplitude of $\pm 10\%$. As with the single wire calculations in Section 2.3, once acceleration of the shell commences, the early phases of instability behavior are characterized by a gradual progression from rapid growth of short wavelength instabilities seeded by the cell-by-cell perturbation to longer wavelength, larger amplitude instabilities. The dominant wavelength at late times was ~1.5 mm. At 170 ns, the "bubbles" blown by the magnetic field start to penetrate through the plasma shell. Axial flow of material away from the tip of the bubble at $z = 7$ mm means that the mass per unit length of this region is low and once it breaks through the shell, it is rapidly accelerated down to the axis. The stagnation of this bubble marks the start of the X-ray power output (see Fig. 18a). The rise time of the radiation pulse (~25 ns) is then given by the time it takes the rest of the mass, which now exists in the form of disc-like radial spikes, to reach and stagnate on the axis. In this particular case, the relatively low radiation loss rate of aluminum means that not all the kinetic energy of implosion is dissipated as radiation, allowing the stagnated plasma to get hot and expand. This rebound is then followed by a second compression that in this case produces a second radiation burst of higher intensity than the first.

The factors determining the rise time (and hence the peak power) of the radiation pulse can best be understood by

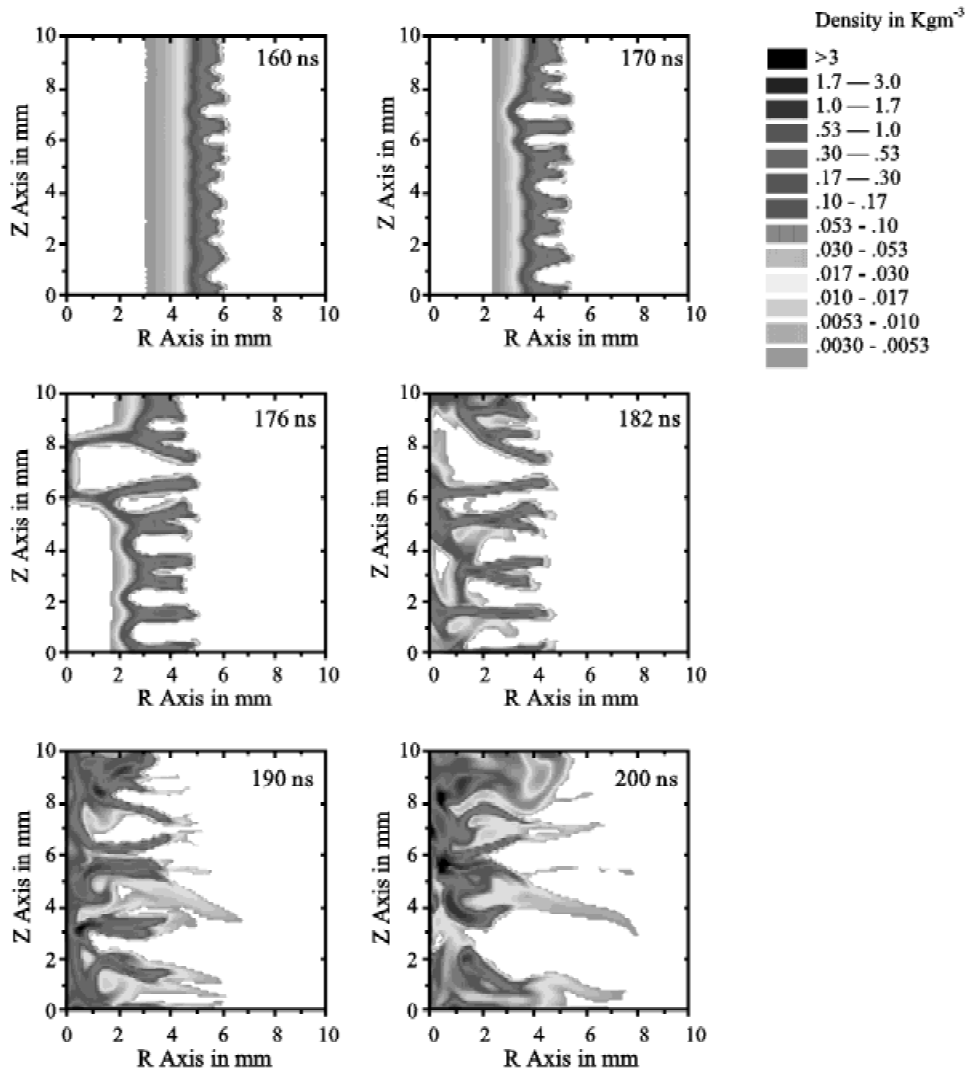

Fig. 17. A sequence of mass density contour maps showing the Rayleigh–Taylor instability growing in a 2-D (r–z) plasma shell driven by the MAGPIE generator.

https://doi.org/10.1017/S0263034601193031 Published online by Cambridge University Press

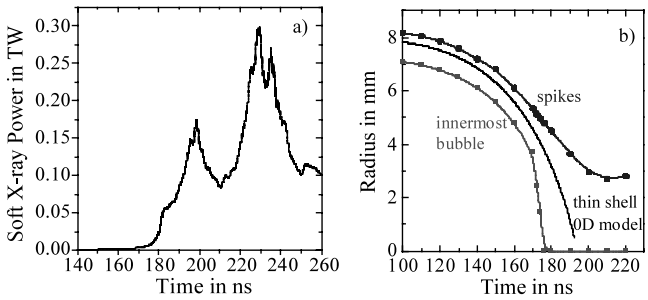

Fig. 18. (a) Total soft X-ray power *versus* time, and (b) radii *versus* time for the innermost bubble and the spikes from the 2-D (*r*–*z*) simulation in Figure 17.

considering the trajectories of the bubbles and spikes and comparing them with the trajectory of a thin shell (obtained using the 2-D (*r*–*z*) code with zero perturbation amplitude; see Fig. 18b). As with the $m = 0$ instability in Section 2.3, rather than following a contorted path in and out of the spikes and bubbles, the current follows the first straight path available and flows through the bubbles. Thus the first development of a large amplitude, nonlinear instability (here at ~170 ns) is followed by acceleration of the bubbles ahead of the average trajectory. Conversely, the spikes become current-free and therefore force-free, stop accelerating, and cruise towards the axis at constant velocity. In this particular case, this break point in the trajectory occurs at a radius of ~4 mm. The bubbles are rapidly accelerated and start to reach the axis ~5 ns later, the spikes continue with a constant velocity of -1.3×10^5 ms^{-1} and therefore reach the axis ~30 ns later, so that the radiation pulse rise time is ~25 ns.

For high wire number wire array experiments, the overall effect of averaging the $m = 0$ instabilities in individual wires results in lower Rayleigh–Taylor perturbation amplitudes than is used in the simulations shown in Figure 17. As a consequence, large amplitude development of the Rayleigh–Taylor instability does not occur until the shell is much closer to the axis. The time difference between bubbles and spikes hitting the axis is therefore less and the radiation pulse rise time is smaller. In tungsten wire arrays, the majority of the kinetic energy of implosion is dissipated during the first radiation pulse, there is little or no rebound, and second radiation pulses are unusual. However, in tungsten implosions as in the aluminum implosion described in Figure 17, despite the considerable $m = 0$ instability which occurs after stagnation, the plasma remains confined on the axis. During this phase the turbulent action of the $m = 0$ instability allows further energy to be extracted from the magnetic field and converted into heat and thus into radiation (Rudakov *et al.*, 2000). The radiation pulse therefore consists of two parts, with an approximately Gaussian pulse (whose total energy is roughly equal to the kinetic energy of implosion) followed by a much longer, lower power tail. While this second component may in fact double the total soft X-ray yield, it is not particularly useful for ICF applications, where optimum power is the primary requirement.

5.2. The effect of the 3-D plasma formation phase on 2-D (*r*–*z*) Rayleigh–Taylor development

To address the issue of the experimentally observed dependence of radiation pulse rise time on wire number, we can in theory use the results of Section 2 to provide initial perturbation amplitudes and the results of Section 3 to provide radial profiles for the final implosion. At the time of press, this work was still in progress and more complete results will be the subject of a future publication. Some indication of the relative importance of the mass injection phenomena described in Section 3 and the $m = 0$ instabilities in each wire described in Section 2 can, however, be obtained more simply.

Comparing 1-D simulations of the implosion phase using either the radial profiles obtained in Section 3 or a 1-mm-wide uniform shell (as used in Sec. 5.1) as initial conditions shows little difference in the final radiation output pulse. The arrival of a significant fraction of the mass prematurely on axis produces low-level precursor radiation but, in both cases, the rapid final implosion of the remaining mass and, in particular, the compression of this plasma by the magnetic field results in unrealistic levels of compression and subnanosecond radiation pulse rise times at the main stagnation. In 2-D, the growth of the Rayleigh–Taylor instability has been shown to be reduced in pinches with distributed radial profiles and for the correct choice of initial conditions can even be completely suppressed (Velikovich *et al.*, 1998). An additional factor is that the discrete wire implosion trajectory described in Section 3, which consists of a fraction of the mass imploding at higher velocity, has a lower integral number of growth times than the implosion of a thin shell. Therefore contrary to experimental observations (Sanford *et al.*, 1999), based on 2-D (*r*–*z*) stability considerations, the presence of mass injection implies less instability development for lower numbers of wires. However, the 3-D behavior observed in Section 1.2 suggests that this may be an oversimplification.

Perhaps a more appropriate scaling of Rayleigh–Taylor instability level with wire number comes from considerations of the $m = 0$ instability in the individual wire plasmas. For low wire numbers, the penetration of the wire core by the necks of the $m = 0$ instability results in 100% modulation of the mass per unit length *versus* axial position. Taking results for the mass per unit length versus *z*, from Figure 7b, and averaging for 24 wires with random phases between the instabilities, yields an average global perturbation. Fourier analysis of this shows a spectrum of modes with components not only due to the dominant wavelength of the $m = 0$ instability (characterized by the distance between necks) but also shorter wavelength components associated with the size of the necked regions and the size of features in the flares. Thus the effective perturbation applied to the implod-

https://doi.org/10.1017/S0263034601193031 Published online by Cambridge University Press

ing plasma is of much longer wavelength than the random density perturbations used in 2-D (r–z) simulations. In general, with small numbers of wires, the amplitude of these modes follows the $1/\sqrt{N}$ scaling suggested by Haines (1998), where N is the number of wires. For higher wire numbers however, the instabilities do not penetrate the core before the implosion starts and hence the mass modulation level in each wire becomes a function of current per wire (i.e., number of wires in the array). Thus, for large numbers of wires, the dependence of the average global-perturbation amplitude on the wire number is much stronger than $1/\sqrt{N}$. Thus, there appears to be a critical wire number, associated with whether or not the individual wire cores are penetrated by $m = 0$ instabilities, that controls the dependence of the Rayleigh–Taylor perturbation amplitude (and the X-ray pulse rise time) on the number of wires in the array.

However, as discussed in Section 2.5, in experiments (Lebedev *et al.*, 1999) the $m = 0$-like instabilities in individual wires are decidedly three-dimensional. Therefore, addressing the issue of the origin and form of the Rayleigh–Taylor perturbation, will require high-resolution 3-D simulations of several wires in the array.

6. SUMMARY AND CONCLUSIONS

A series of different resistive MHD codes have been used to study the different phases of wire array z-pinch evolution.

By the addition of relatively simple models for the equations of state and dense plasma transport coefficients into a 2-D (r–z) resistive MHD code, we have obtained a fair reproduction of experimental data for single, metallic-wire z pinches. While the use of this code for modeling single wires in an array is limited by the absence of 3-D effects, it does allow the effects of the $m = 0$ instability to be scaled with the number of wires. Data from a wire number scan with aluminum wire arrays on the SATURN generator suggest that the observed sharp transition to high X-ray power at around 40 wires (Sanford *et al.*, 1999) corresponds to a sharp decrease in $m = 0$ perturbation amplitude and, hence, a sharp decrease in the seed perturbation for the Rayleigh–Taylor instability. The results also show a trend towards increased merger of adjacent wire plasmas as the number of wires is increased. If a substantial increase in the expansion of the wire cores could be obtained, it would result in the complete merger of adjacent wires and a shell-like implosion. Simulations, using the cold-start model described in Section 2, suggest that this can be achieved (in a 40-mm-diameter array of 240 7.5-μm-diameter tungsten wires on Z) by applying a prepulse current of $\sim$1 kA per wire over a 100-ns time scale and then waiting 500 ns before applying the main current pulse. The low-level current provides enough energy to vaporize the wire cores, which then expand at roughly their sound speed ($\sim$500 ms^{-1}) and cross the interwire gap in $\sim$500 ns. Applying such a slowly rising, low-amplitude current would also result in negligible instability growth during the prepulse phase. The large diameters of the wire cores will also result in substantial reductions in $m = 0$ growth during the main current pulse, leading to lower levels of Rayleigh–Taylor perturbation and more symmetric implosions.

Two-dimensional simulations in the r–θ plane show how the slow rate of wire core ablation and the topology of the magnetic field controls the radial and azimuthal structure of wire array z-pinch implosions. Injection of material between the wires and into the interior of the array in the form of radial plasma streams is a perennial feature of all wire arrays. However, with large numbers of wires and small interwire gaps, the effects of these phenomena are reduced. These radial plasmas streams have an obviously detrimental effect on many ICF applications, in particular dynamic hohlraum applications (Matzen, 1997), where their bombardment of the centrally located foam buffer will create significant radiative preheat of any target capsule embedded within it. The precursor plasma produced and confined by the radial plasma streams, however, exhibits remarkable uniformity, stability, and longevity and offers enormous potential as a plasma-physics test-bed.

In nested wire arrays, the density and velocity of the stream of outer-array material determine the heating and expansion rate of the inner array wires. The size to which the inner array wires expand during this bombardment, along with the degree of magnetic flux compression, determine the level of momentum transferred during the collision and, thus, control the subsequent implosion trajectory. Results suggest, that for tungsten wire array experiments on Z, large interwire gaps ($>$1.5 mm) are required in the inner array in order to access the transparent inner mode in which the outer array material passes through the gaps in the inner array. This configuration offers the potential for achieving higher X-ray powers (Davis *et al.*, 1997; Terry *et al.*, 1999; Lebedev *et al.*, 2000*a*).

Two-dimensional (r–z) simulations of the final implosion phase show how the Rayleigh–Taylor instability leads to an increase in the radial width of the imploding plasma and hence an increase in the radiation pulse rise time and a decrease in the maximum radiation output power. Since in large wire number arrays, the final stages of implosion are largely symmetric in the azimuthal direction, the reduction of the problem to 2-D (r–z) coordinates might appear to be justified, provided the correct initial perturbation levels and radial profiles are used. However, one cannot simply use the 2-D (r–z) simulations of Section 2 and the 2-D (r–θ) simulations of Section 3 to determine the perturbation level and radial profiles, respectively. As is clear from the experimental data (Lebedev *et al.*, 2001), the evolution of the plasma is decidedly three-dimensional and the development of $m = 0$-like instabilities in each wire plasma and the mass injection phenomena cannot be considered in isolation. In addition the reasons why the transition from uncorrelated instabilities in each wire plasma to a global Rayleigh–Taylor instability is accompanied by a fourfold increase in wavelength is not at all understood. There therefore remains

https://doi.org/10.1017/S0263034601193031 Published online by Cambridge University Press

a significant need for three-dimensional simulations of either one or several wires in an array which can model the progression from cold start right through to the final implosion phase with high spatial resolution.

ACKNOWLEDGMENTS

The authors gratefully acknowledge many interesting discussions on the physics of wire arrays with a large number of scientists from Sandia National Laboratories, Cornell University, Naval Research Laboratory, Los Alamos National Laboratory, and Lawrence Livermore Laboratory and, in particular, with Drs. R.B. Spielman, C. Deeney, M.K. Matzen T.A. Mehlhorn and T.W.L. Sanford from SNL. We are also particularly grateful to Prof. D.A. Hammer, Dr. S.A. Pikuz and Dr. T.A. Shelkovenko for providing some of the comparative experimental data.

This work was supported by AWE Hunting-BRAE through the William Penney Fellowship scheme, by Sandia National Laboratories (contract number BF-6405) and by the U.S. DOE under contract number DE-FG03-98DP00217.

REFERENCES

Beg, F.N. *et al.* (1997). *Plasma Phys. Controlled Fusion* **39**, 1.
Chittenden, J.P. (1995). *Phys. Plasmas* **2**, 1242.
Chittenden, J.P. *et al.* (1997*a*). *Phys. Plasmas* **4**, 2967.
Chittenden, J.P. *et al.* (1997*b*). *Phys. Plasmas* **4**, 4309.
Chittenden, J.P. *et al.* (1999). *Phys. Rev. Lett*. **83**, 100.
Chittenden, J.P. *et al.* (2000). *Phys. Rev. E.* **61**, 4370.
Christiansen, J.P. *et al*. (1974). *Comp. Phys. Comm*. **7**, 271.
Davis, J. *et al*. (1997). *Appl. Phys. Lett.* **70**, 170.
Deeney, C. *et al.* (1997). *Rev. Sci. Instrum.* **68**, 653.
Deeney, C. *et al.* (1998). *Phys. Rev. Lett.* **81**, 4883.
Desjarlais, M. *et al.* (2001). *Contrib. Plasma Physics* **41**, 267.
Douglas, M.R. *et al.* (2000). *Phys. Plasmas* **7**, 1935.
Dyos, G.T. & Farrell, T. (1992). *Electrical Resistivity Handbook*. London: Peter Peregrinus Ltd.
Figura, E.S. *et al*. (1991). *Phys. Fluids B* **3**, 2835.
Guskov, S.Y. (1998). *JETP Lett.* **67**, 559.
Haines, M.G. (1998). *IEEE Trans. Plasma Science* **26**, 1275.
Hammer, J.H. & Ryutov, D.D. (1999). *Phys. Plasmas* **6**, 3302.
Hammer, J.H. *et al.* (1999). *Phys. Plasmas* **6**, 2129.
Ivanenkov, G.V. (1998). *JETP* **87**, 663.
Kalantar, D. & Hammer, D. (1993). *Phys. Rev. Lett.* **71**, 3806.
Kershaw, D.S. (1978). *J. Comp. Phys*. **26**, 43.
Kirzhnits, D.A. (1959). *Sov. Phys. JETP* **8**, 1081.
Latter, R. (1955). *Phys. Rev*. **99**, 1854.
Lebedev, S.V. *et al.* (1998*a*). *Phys. Plasmas* **9**, 3366.
Lebedev, S.V. *et al.* (1998*b*). *Phys. Rev. Lett*. **81**, 4152.
Lebedev, S.V. *et al.* (1999). *Phys. Plasmas* **6**, 2016.
Lebedev, S.V. *et al*. (2000*a*). *Phys. Rev. Lett.* **84**, 1708.
Lebedev, S.V. *et al*. (2000*b*). *Phys. Rev. Lett*. **85**, 98.
Lebedev, S.V. *et al*. (2001). *Laser Part. Beams* **19**, 355 (this issue).
Lee, Y.T. & More, R.M. (1984). *Phys. Fluids* **27**, 1273.
Matzen, M.K. (1997). *Phys. Plasmas* **4**, 1519.
Noh, W.F. (1987). *J. Comp. Phys*. **72**, 78.
Peterson, D.L. *et al.* (1999). *Phys. Plasmas* **6**, 2178.
Pikuz, S.A. *et al.* (1999). *JETP Lett.* **69**, 377.
Post, D.E. *et al*. (1977). *Atomic Data and Nuclear Data Tables* **20**, 398.
Rudakov, L.I. *et al.* (2000). *Phys. Rev. Lett. **84***, 3326
Ruiz-Camacho, J. *et al.* (1999). *Phys. Plasmas* **6**, 2579.
Sanford, T.W.L. (2001). *Laser Part. Beams* **19(4)**.
Sanford, T.W.L. *et al.* (1996). *Phys. Rev. Lett*. **77**, 5063.
Sanford, T.W.L. *et al.* (1999). *Phys. Plasmas* **6**, 2030.
Springer, P.T. *et al*. (1997). *J. Quant. Spectrosc. Radiat. Transfer* **58**, 927.
Tarter, C.B. (1977). *J. Quant. Spectrosc. Radiat. Transfer* **17**, 531.
Terry, R.E. *et al.* (1999). *Phys. Rev. Lett*. **83**, 4305.
Velikovich, A.L. *et al.* (1998). *Phys. Plasmas* **5**, 3377.
Whitney, K. *et al.* (1997). *Phys. Rev. E* **56**, 3540.
Youngs, D.L. (1982). *Numerical Methods for Fluid Dynamics* (Morton, K.W. and Baines, M.J., Eds.) New York: Academic Press.